Max-Planck-Institut
für Kolloid- und Grenzflächenforschung

Universität Potsdam

Synthesis and Characterization of Transition Metal Nitrides and Carbides for Catalysis and Electrochemistry Application

Masterarbeit im Fachbereich Chemie an der Universität Potsdam

Sarah Metzke

14.10.2013

Prüfer:
Dr. Cristina Giordano

Prüfer:
Prof. Dr. Andreas Taubert

Published online at the
Institutional Repository of the University of Potsdam:
URL http://opus.kobv.de/ubp/volltexte/2014/6983/
URN urn:nbn:de:kobv:517-opus-69835
http://nbn-resolving.de/urn:nbn:de:kobv:517-opus-69835

Zusammenfassung

Im Rahmen dieser Arbeit wird sowohl die Synthese von Mangannitrid- und -oxid-Nanopartikeln, als auch die Synthese verschiedener Metall- und Legierungsnanopartikel untersucht. Einen Schwerpunkt stellt dabei die Optimierung der Synthese unter den Gesichtspunkten der Nachhaltigkeit dar, was sich insbesondere in der Verwendung diverser nachwachsender Rohstoffe als Kohlenstoffquelle äußert.

Für eine mögliche Anwendung in Akkumulatoren werden mit Graphit ummantelte $MnN_{0.43}$-Nanopartikel mit einer großen Oberfläche (79 m^2g^{-1}) synthetisiert. Diese werden exemplarischen Ladezyklen unterzogen, wobei eine strukturelle und auch elektrochemische Stabilität festgestellt werden kann. Eine Mischung der Mangannitride mit Manganoxiden führt zu einer weiteren Verbesserung der Ladekapazität und einer weiteren Oberflächenvergrößerung (93 m^2g^{-1}). Die Langlebigkeit der Strukturen wird durch die Einbettung der Nanopartikel in Kohlenstoff unterstützt und kann zu einer Anwendung als Anodenmaterial in den heutzutage vielfach verwendeten Lithiumionen-Akkus führen.

Im Sinne der Nachhaltigkeit ist auch die Entwicklung von Katalysatoren. Dabei soll insbesondere die Verwendung von Lignin, was als Bestandteil vieler Pflanzen zwar leicht verfügbar, aber unglücklicherweise bisher chemisch unverwertbar ist, fokussiert werden. Um sich diesem Ziel zu nähern und entsprechende Mechanismen zur Reduktion des Lignins zu entwickeln, werden in dieser Arbeit zunächst verschiedene Kohlenstoffquellen (wie Cellulose, Sucrose und Glucose) zur Synthese von reduktiven Katalysatoren untersucht. Der Kohlenstoff dient dabei sowohl als preiswertes Reduktionsmittel für Metallsalze zur Gewinnung von Metallnanopartikel als auch zur Stabilisierung ebendieser. Es werden vielfältige Legierungen mit Nickel (z.B. $Pd_{0.9}Ni_{0.1}$, $Pd_{0.5}Ni_{0.5}$, $Fe_{0.5}Ni_{0.5}$, und $Cu_{0.5}Ni_{0.5}$) aber auch ternäre Carbide (z.B. $Mn_{0.75}Fe_{2.25}C$) erhalten, die schon in ersten Alkylierungs- und Hydrierungsreaktionen ein großes Potential als Katalysatoren zeigen.

Um die erhaltenen Nanopartikel in zukünftigen Anwendungen nutzbar zu machen, ist eine ausführliche Charakterisierung unabdingbar. Auch die Ergebnisse der zahlreichen durchgeführten Analysen werden in dieser Arbeit zusammengestellt und bilden gemeinsam mit den optimierten Syntheserouten einen tiefgreifenden Überblick über dieses Forschungsfeld.

Contents

1. Introduction

1.1. Green Chemistry

Nowadays it is very important to design or improve chemical processes, materials or systems following a "green chemistry" approach. The 12 Principles of Green Chemistry, defined by *Anastas* and *Warner*,[1],[2],[3] are recommending: waste prevention, reduction of hazardousness, the use of less toxic solvents and precursors, efficient energy use (reactions at ambient temperature and pressure if possible), renewable precursors, one-pot syntheses to reduce derivatizations or purifications steps, selective catalysts and the use of safe substances in order to prevent accidents. The concepts mentioned above are important in order to save resources, energy, time and money.

Almost all industrial processes are requiring the use of catalyst, but most of the common syntheses reported in literature involve the use of toxic solvents and are usually very specialized approaches only valid for one system. The goal of this work was to exploit green synthesis approaches, which can be used for the preparation of different systems. These approaches do not demand purification, can be conducted in water, use safe and sustainable chemicals (i.e. not expensive). The whole system including precursors and the products is stable and easy to handle. Furthermore the syntheses are not very sensible and use relatively mild conditions.

One key point to improve sustainability is to find an easy way to recover and recycle substances. Precious metals for example are often used in catalysis; unfortunately, they are hard to recover. As wastes they are unwanted since they pollute the environment. The use of ferromagnetic catalysts (e.g. iron, cobalt or nickel) is a smart way to simplify the recovery process,[4] as they could be easily recovered from the reaction by magnetoseparation.[5],[6],[7]

In conclusion, the best would be a one-pot synthesis with the possibility of scale-up in the interest of application, for example in batteries or catalysis. Those two applications were chosen for the synthesized particles because they already proved to be promising for similar systems synthesized by our group.[8],[9],[10],[11]

1.2. Nanoparticles in Catalysis

Nanoparticles are getting progressively more common in catalytic applications. One basic reason is the need of less material compared to the bulk phase to get the same catalytic activity. Furthermore, while the properties of bulk materials are mainly related to their volume, nanoparticles are primarily influenced by their surface characteristics due to their high surface to volume ratio. Reducing the size to the nano-scale can also lead to an improvement or even a complete change of properties, leading to size-dependent properties and different activity. While for instance bulk gold is "inert" on the macro-scale, it becomes a catalyst when the size is reduced to nano-size.[12]

Heterogeneous catalysis profits from an easy recovery of the metal and possible high temperature processes. Although homogenous catalysts are usually more selective, their separation and recyclability is lacking; moreover, they are not stable at high temperatures.[12] In terms of green chemistry, catalysts should be environmental-friendly (e.g. phosphine-free), easy to recover, recyclable, selective and efficient even at mild conditions. These demands are mostly fulfilled by transition-metal nanoparticles. One major drawback of most synthetical approaches is the particle stabilization. A classical chemical support for catalysts is charcoal (e.g. Pd/C), which was tried to be adapted as a support for nanoparticle. This carbon had to be prepared and modified in order to get the desired porosity and pore size distribution as well as a high surface area. [12]

This thesis will present different carbon supported metal(0) and alloy nanoparticles synthesized in a one-pot approach forming carbon embedded nanoparticles that are stable in air and solvents. Since the majority of the systems contain magnetic particles, when applied as catalysts, they can be easily recovered by magnetic separation. In this thesis a variety of carbon embedded nano-composites were produced and characterized, including Ni^0 nanoparticles and a variety of metal alloys like $Pd_{0.9}Ni_{0.1}$, $Pd_{0.5}Ni_{0.5}$, $Fe_{0.5}Ni_{0.5}$, $Cu_{0.5}Ni_{0.5}$ and $W_{0.15}Ni_{0.85}$. The versatility of the synthesis was explored further not only to produce metal(0) and metal alloy nanoparticles but also ternary carbides. In particular $Mn_{0.75}Fe_{2.25}C$ was synthesized and also tested for its catalytic properties. All of these nano-composites were made by an easy approach, described further in chapter 3.2, using a carbothermal reduction of a reaction mixture containing only a water-soluble metal salt, water and a saccharide. The basic route was set by Stefan Glatzel using cellulose, but was only applied in

catalysis to give some preliminary results.[13] It is the objective of this thesis to explore the possibility to make the surface of the nanoparticles available for catalysis and to adapt the route towards other systems. Characterization and catalytic properties of the materials will be discussed in detail in chapter 5.

1.3. Nanoparticles in Batteries

Among the already discussed conveniences of nanoparticles, some more can be stated for the use in lithium-ion battery systems. Their small size is a major advantage, since alternative materials should reduce size and weight of the batteries used, which is important for the miniaturization of portable systems. The small dimensions of the particles are reducing the paths for ions and electrons within an electrode, leading to fast reactions and thus to shorter charging and discharging times. The high surface area increases the contact of the electrode towards the electrolyte and is therefore contributing to a faster movement of the lithium ions. Thermodynamically, reducing the size of a bulk material towards nano-size can lead to a change of electric potential even for systems that are inactive as bulk material.[14]

1.4. Nitrides and carbides

Interstitial alloys between carbon or nitrogen and early transition metals are forming compounds with metal-like character due to their similarity in the closed-packed crystal structures. As bulk-materials, metal carbides and nitrides are known for their high chemical stability and multifaceted chemical and physical features.[15] Indeed, nitrides and carbides are known for their ceramic-like behavior when it comes to resistance against corrosion, high melting points and hardness, but metal-like characters when it comes to electric and magnetic properties.[16],[17] These features are already employed by using titanium nitride as steel coating in daily life, while group 13 nitrides find application in semiconductor devices.[18],[19],[20] Finally, due to their metallic characters, their catalytic activity appears to be similar to the one of the noble metals (Pd, Pt), which makes them interesting systems to replace precious metals in catalytic reactions.[16]

A review of the literature on nitrides and carbides shows that these materials are far less studied than oxides for instance. One reason that might explain this lack of interest can be found in their preparation. Up to a few years ago it was common to produce nitrides as bulk phase under high pressure ammonia and/or at very high temperatures, which often lead to a

mixture of different nitrides, also because of the problematic reaction between solid and gaseous phase. A possible approach is the urea-glass route, a sol-gel based process which was reported by Giordano *et al.*[17],[20],[21] This approach is very general and can be employed to produce a variety of nitrides, carbides and oxynitrides.

In this thesis manganese nitride and manganese nitride/oxide nano-composites embedded in carbon will be synthesized using the urea-glass route, further described in chapter 3.1. These systems were subject to battery tests using the nano-composites as novel electrode materials for lithium ion batteries[15] and will be compared to the material before discharge. Characterization and the application in batteries will be further discussed in chapter 4.

1.5. Characterization and Application

The subject of this thesis is the synthesis of several materials and especially their characterization with just some first approaches towards application. Indeed, it is very important to fully understand the characteristics of a material to comprehend its properties. In order to modify and improve systems, it is important to perceive how several reaction parameters influence the properties of the final product.

Furthermore, many different systems were tried out to find the most promising one and to test the versatility of the synthesis approach. The synthesized materials were only barely characterized or tested before. Hence, optimization was one of the main targets. Another main part of the thesis will therefore cover characterization including advanced techniques (e.g. EELS), which leads to deeper investigation. As a first approach, some of the materials were explored further in the means of application. These tests could be considered as preliminary, but already proved to be very promising.

2. Analytical techniques

2.1. Electron microscopy

The electron microscope makes it possible to observe particles in the nanometer range.[22] The resolution *d* of a microscope can be calculated according to *Abbe* equation (1). In this equation λ indicates the wavelength, *n·sinα* is the numerical aperture.

$$d = \frac{0.61 \cdot \lambda}{n \cdot \sin \alpha} \quad (1)$$

For a light microscope this equation limits the resolution, based on the minimum wavelength of the visible light (≈400 nm), to objects larger than 200 nm. In order to visualize smaller objects, it is possible to use electron beam radiation. The wavelength λ of an electron can be calculated according to the De Broglie's equation (2). Here *h* is the Planck constant, m_e is the electron weight and *v* is the velocity.

$$\lambda = \frac{h}{m_e \cdot v} \quad (2)$$

The velocity of an electron is dependent on the acceleration voltage of the microscope. Hence, the acceleration voltage determines the wavelength of an electron with the charge *e* and an acceleration voltage *V* according to equation (3).

$$\lambda = \frac{h}{\sqrt{2 \cdot m_e \cdot e \cdot V}} \approx \sqrt{\frac{1.5}{V}}\ [nm] \quad (3)$$

With an acceleration voltage of 120 kV this wavelength would be 0.0035 nm. The maximum possible resolution cannot be reached in reality due to the lens design and the resulting chromatic and spherical aberrations (distortions). The theoretical resolution of electron microscopes is approximately $d_{theo} = 0.2$ nm, when the aberrations are taken into consideration.[22]

2.1.1. Transmission electron microscope

The first step in the TEM is the generation and acceleration of an electron beam in the electron gun. Since contaminations within the electron gun (atmospheric oxygen etc.) would harm the cathode, high vacuum is needed for every measurement. The electron beam is then focused onto the sample using condenser lenses. The samples are required to be transparent for the electron beam. This limits the thickness of the sample to 100 nm, letting a small section of the electron beam through the sample. When an accelerated electron

beam reaches a sample, different interactions can occur. These various interactions (e.g. directly transmitted electrons, elastic scattering, inelastic scattering, X-rays) can be used to get information about the sample using different analytical techniques (e.g. EELS, EDX). In the classical TEM, directly transmitted electrons are forming the final image after passing further lenses. The contrast of the final image is due to the mass-thickness-contrast. Heavy elements, as well as thick parts of the sample appear to be dark, light elements and thin parts bright.

When a sample is too thick, the electron cannot pass through and imaging is impossible. Here the method of ultramicrotomy can help to prepare the samples embedding them in a hardening resin and slicing it into small sections called ultramicrotomes after the hardening process.[23],[24],[25]

SAED

Since the wavelength of the electron beam is a lot smaller than the distance between the atoms of a sample, the crystal lattice can act as a diffraction grating. Some of the electrons are diffracted to specific angles. The selected area electron diffraction (SAED) can either show regular spots for the diffraction of a single crystal particle or ring patterns resulting from large numbers of randomly oriented crystalline particles. From the resulting patterns, the crystal lattices can be determined according to Bragg. SAED is similar to XRD, but it is possible to investigate just a small selected area of the sample.[23]

HRTEM

The basis for high-resolution TEM is phase contrast imaging and depends on the use of interference between electron waves. There is a small difference in the phase when an electron is leaving the bottom of a sample due to scattering within the sample. These phase contrast effects play an important role in the imaging of lattices. HRTEM can resolve detailed structures and can provide information about the periodicity of the crystal lattice.[24]

EELS

In contrast to classical TEM imaging, which uses elastic scattering and transmission, electron energy loss spectroscopy uses inelastic scattering of the primary electron beam. The EELS detector catches and disperses the inelastically scattered electrons after passing the sample. Electrons with the same energy are focused to the same spot of the detector. The spectrum shows the energy distribution of the passing electrons. EELS is working best for low atomic

number elements because the excitation edges are sharper and gives information about atomic composition and chemical bonding.[26]

EDX

Energy-dispersive X-ray spectroscopy is using, as already indicated by the name, X-ray scattering resulting from inelastic scattering of the electron beam with the sample electrons. If, due to the electron beam, an electron from in an inner shell of the sample is excited and ejected, an electron from an outer shell (higher energy) will fill the hole that was created. The difference of the electron energies is getting released as an X-ray. The energy (representative for a specific element), number and distribution of these X-rays can be detected by an EDX-detector attached to the electron microscope. EDX can help to identify the elemental composition of a sample, but is very limited due to overlapping peaks and the difficulty to measure light elements.[26]

2.1.2. Scanning electron microscope

Scanning electron microscopy (SEM) is a technique that can three-dimensionally visualize the surface structure of a sample using further corrections for the spherical aberration. In this technique the electron beam is not passing though the sample, but scanning the surface point-by-point. The interactions of the electron beam with the sample are resulting in secondary electrons, which can be detected. The more electrons are detected, the higher is the intensity in the final picture. Heavy elements containing a large number of electrons are therefore represented by brighter areas, while light elements are represented by dark areas. The preparation of samples investigated by REM usually includes sputtering with a conductive material (e.g. gold). Since the systems investigated in this work are conductive themselves, this step is not needed.[27]

2.2. Nitrogen sorption

Since a high surface area is a very important feature for catalysts, it is necessary to get some information about the surface characteristics of the samples. The principle of nitrogen sorption measurements is the physisorption of nitrogen molecules onto a sample surface and determining the amount, which is needed to form a complete monolayer on the surface. At 77 K the amount of adsorbed nitrogen as a function of the pressure p/p_0 is recorded as an isotherm. The evaluation of the data can be done by the model of Brunauer, Emmet and Teller (BET) in order to receive the apparent BET surface area from the relative pressure

range of 0.05 – 0.3. Furthermore nitrogen sorption measurements can show average pore volumes and distributions. [25],[28]

2.3. Elemental analysis (CHN)

The elemental analysis of light elements (C, H, N, S, O) is carried out using catalytic combustion under an oxygen flow and high temperatures. The gas mixture resulting from the high temperature decomposition is then separated using specific adsorption columns and determined with a thermal conductivity detector.[29]

2.4. X-Ray diffraction

The determination of crystalline phases and powders is carried out by X-ray diffraction analysis, which relies on the basic interaction between X-ray radiation and the periodically arranged atoms of the crystal lattices. A constructive interference of the diffracted waves occurs only when the path difference is a multiple *n* of the wavelength λ (CuK_α-radiation) with the angle of incoming radiation θ and the distance between the lattice planes d_{hkl} according to the Bragg equation (4).

$$n \cdot \lambda = 2 \cdot d_{hkl} \cdot \sin\theta \tag{4}$$

The advantage of powder diffraction in contrast to the single crystal diffraction, where every single lattice has to be investigated individually, is the random distribution of the crystals. Therefore, different crystal lattices can be seen at once. For identification purposes, the signals can be matched according to the ICDD-database. If the crystallites are very small, a broadening of the X-ray reflex occurs. The crystallite size d_{hkl} can be estimated using the Scherrer-equation (5) with the form factor *K* (estimated as 1 for spherical particles), the wavelength λ and the full width at half maximum *FWHM* of the peak intensity at the Bragg angle θ.

$$d_{XRD} = \frac{K \cdot \lambda}{FWHM \cdot \cos\theta} \tag{5}$$

The Scherrer equation is only an estimation since not only the particle size, but also the level of crystallinity plays a role in the shape of the signal. Crystalline particles are giving sharp signals, while amorphous compounds only give very broad signals with smaller intensity.[25],[30]

2.5. ICP-OES

Qualitative and quantitative investigations of trace metals can be carried out by inductively coupled plasma optical emission spectrometry. The sample is atomized and excited in hot

argon plasma, emitting electromagnetic radiation of wavelengths characteristic for the element. The emission intensity is connected to the element concentration in the sample.[27]

2.6. H-Cube Pro Reactor

The hydrogenation reactor, which is used for catalytic tests, enables continuous hydrogenation reactions. The substrate is combined with hydrogen in a continuous flow and can be heated up to 150 °C and pressurized to 100 bar of H_2. The hydrogen needed is generated *in-situ* from electrolysis of water, making the reactions less hazardous than storing a large amount of hydrogen in high pressure gas cylinders. The substrate/hydrogen mixture is then sent through the cartridge, which contains the packed catalyst. The eluted product can be collected continuously. The reaction conditions can be easily modified and the catalyst recycled effortlessly.[31]

2.7. GC-MS

The GC-MS combines the chromatographic features of gas chromatography and the detection by mass spectrometry in order to identify and quantify substances within a sample. First the samples are injected into an inert gas stream of helium before they are passed through a column packed with a stationary phase. Differences in the separation of the analyzed substances are due to the absorptive interaction between the compound in the mobile phase (gas stream) and the stationary phase leading to different retention times. The compounds are ionized in high vacuum after passing the chromatographic column. Afterwards the ions and their fragments are sent through a magnetic mass analyzer, which measures the amount of each selected ion in a detector.[32]

2.8. Raman

If molecules are irradiated by monochromatic light, a major part of the light will be scattered elastically exciting the molecules to a virtual electronic state and immediately emitting a photon and falling back to the ground state. The photon energy is equal to the one of the approaching light (Rayleigh scattering). Additionally, it is also possible that the molecule falls back from an excited electronic state to an electronic state that is higher (Stokes scattering) or lower than the ground state (Anti-Stokes scattering). The energy difference of the photons emitted by inelastic scattering corresponds to vibrational states of the molecule and can be identified by their Raman shifts.[30]

3. Synthesis

Commonly, the synthesis of nano-materials is divided into two main approaches, which are called “top-down” and “bottom-up”. In the “top-down” concept a bulk material is split into smaller parts by using approaches like ball milling, sputtering, laser ablation or etching techniques. On the contrary the “bottom-up” approach consists in growing and assembling nanoparticles starting from the atomic or molecular level. The second approach, which includes sol-gel techniques and chemical vapor deposition, is the one used in this thesis.[33]

3.1. Urea-glass-route

Some of the syntheses used in this project are following a sol-gel based procedure called “urea-glass-route”.[20]

In general, a sol-gel synthesis is starting from molecular precursors (usually being a metal salt or a metal alkoxide) forming a metal oxide network via inorganic polymerization (hydrolysis and condensation reactions) in two steps. As a first step the *sol* (colloidal dispersion) is formed before forming the *gel* as a second step upon aging which can then be dried and processed further. With a sol-gel approach it is possible to synthesize bulk oxides, films, fibers and nanoparticles with the advantage of a low processing temperature (RT), a high homogeneity due to the molecular precursors and the possibility to control the morphology by controlling the rate of hydrolysis and condensation. [34],[35],[36]

To apply a sol-gel approach in order to form nitrides and carbides, a second step is needed since those compounds do not form at room temperature. For the urea-glass-route this second step is a carbothermal reduction in presence of a N-/C-source, which is already a known procedure for the formation of nitride and carbide ceramics.[37] In contrast to the classical sol-gel process, instead of using precursors that can polymerize themselves, urea as a nitrogen soruce is forming the gel network.

With the presented urea-glass-route it is possible to obtain carbides, nitrides, oxynitrides and similar mixed derivates.[17] The urea-glass-route is an easy approach that minimizes the use of toxic solvent and needs no purification. In fact, this is a simple and safe method to produce nitrides using urea as nitrification agent replacing high pressure ammonia, required in many other synthesis pathways forming nitrides.

As a first step a gel is formed, which could be considered as a coordinating polymer, held together by hydrogen bridges and Coulombic forces, starting by mixing the metal salt precursor with an alcohol.[17] Then, solid urea or similar nitrogen sources are slowly added as linking agents to the solution, before stirring the mixture for a couple of hours giving a complex of high viscosity also referred to as "gel". In the second step, the resulting gel is thermally treated under a nitrogen flow at 700 – 800 °C, bypassing a glass state, to form solid nitrides or carbides. By varying the reaction conditions like the heating rate/temperature, the nitrogen/carbon source and the urea to metal ratio *R*, the final product can be tuned, varying from nitrides to carbides. In contrast to the already known synthesis approaches to form metal nitride nanoparticles, the resulting products are very stable against oxidation.[17] The used carbon sources for this thesis are shown in Figure 1.

Figure 1: The carbon sources used in the urea approach: urea (left) and guanidine acetate (right)

In this session, two manganese systems will be discussed, one being manganese nitride and the other a manganese oxide/nitride nano-composite. Both systems were already modified but were proven for their reproducibility.[15] For the urea-glass route synthesis, 0.5 g of manganese acetate tetrahydrate are dissolved in 2 g of methanol. It was reported earlier that these are the optimal conditions to have a complexation of manganese with urea.[15] Under stirring conditions, a varying amount of urea or guanidine acetate, the carbon/nitrogen source, is added to the pale yellow solution giving a specific molar ratio of the N-source to manganese (*R*). Using urea, the pale yellow solution is changing to a pale brown solution due to the oxidation of Mn(II) to Mn(III), while the Mn-urea-complex is formed. After 3 hours of stirring, the reaction mixture is transferred into a crucible and calcined at 800 °C under nitrogen with a heating ramp assigned to the formation of the desired product. After cooling down, the solid dark grey product is milled to a fine powder.[15],[38] The gel-like starting material of the manganese-urea-complex and the dark grey powder after calcination and milling are shown in Figure 2.

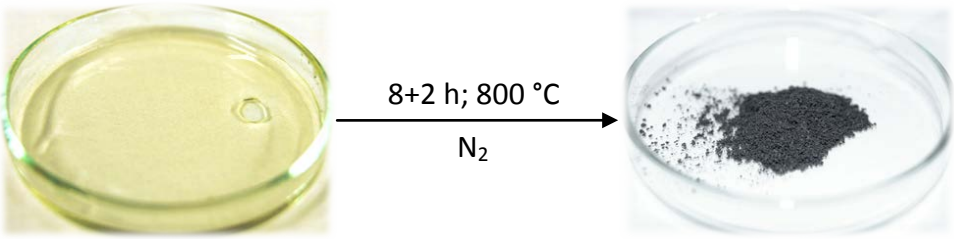

Figure 2: Photographs of the gel-like starting material and the $MnN_{0.43}$ powder after calcination.

As a summary, the optimized reaction conditions, for the investigated systems $MnN_{0.43}$ and $MnN_{0.43}$/MnO are given in Table 1.[15],[20],[38],[39]

Table 1: Overview of the reaction conditions using the urea-route with *R* being the ratio between the N-source and manganese and the heating conditions (first number: heating time to reach temperature, second number: time to maintain temperature).

	C/N-source	Metal salt	R	Heating
$MnN_{0.43}$	Urea	$MnAc_2 4H_2O$	7	800 °C [8+2 h]
$MnN_{0.43}$/MnO	Guanidine acetate	$MnAc_2 4H_2O$	2	800 °C [4+3 h]

The ratios *R* were found to be the optimal one to obtain $MnN_{0.43}$ and $MnN_{0.43}$/MnO particles, which are surrounded by a graphitic shell.[38],[39] Furthermore, the heating conditions were found to be optimal in order to minimize the side product manganese carbodiimide MnNCN.[15],[40] This is an intermediated phase that can still be found in the final product of the single phase manganese nitride samples, especially when it is not heated exactly to 800 °C. It can still be observed with a reaction temperature of 750 °C. Additionally it is important to not choose reaction temperatures higher than 800 °C, otherwise manganese carbides are starting to form.[15]

The resulting systems will be discussed as two possible electrode materials for lithium batteries in chapter 4.

3.2. Saccharide-route

In order to obtain ternary metal carbides embedded in carbon, namely nano-composites, a different synthesis approach was used. This second approach is called saccharide-route. Although the main concept of both, urea- and saccharide-route is a similar one, they will be discussed separately because they are leading to two different systems tested for different applications. The synthetic pathway was already applied earlier, using cellulose as the carbon-source. The reaction conditions, including the temperature and the ratio between two metals were already set by Stefan Glatzel;[13] using cellulose as the carbon source, only the most promising systems were replicated in this thesis. In the present work the route is extended to other carbon sources (sucrose, glucose and lignin). Since all of those carbon sources belong to the class of saccharides, the name "saccharide route" was chosen. A further modification of the route will be done towards other carbon sources and different carbon to metal ratios. In addition, it was possible to also obtain metal or metal alloy nanoparticles embedded in carbon, which are suitable for catalytic applications since the porous materials have got a much higher surface area. In order to prove the versatility of the route, different systems were tested, leading to different nano-composites. These in turn are leading to different applications in catalysis. On the one hand different combinations of metals were used to form different alloys or ternary carbides; on the other hand nickel was used as a model system to evaluate the influence of the carbon source.

In a typical experiment, a saccharide is added under stirring or mechanical shaking to 5 mL of a 0.57 M metal salt solution, obtained by dissolution of 2.87 mmol of the metal salt in 5 mL of water. The amount and the carbon source itself were varied. These experimental details are summarized in Table 2.

Table 2: Summary of the used saccharide amounts.

Ratio C/M	8:1	16:1	33:1
Cellulose	0.64 g	1.27 g	2.54 g
Sucrose	0.67 g	1.34 g	2.68 g
Glucose	0.71 g	1.41 g	2.82 g
amount of carbon	23.5 mmol	47 mmol	94 mmol

In the original (classical) approach the amount of cellulose was chosen to be the maximum amount of cellulose that could be soaked with the metal salt solution, resulting in a 33:1 carbon to metal ratio. The other ratios in Table 2 were chosen to reduce the carbon source

to the half (16:1) and quarter (8:1) of the original amount in order to modify and modify the systems, i.e. reduce the amount of carbon.

The syntheses are conducted directly in crucibles. First, the metal salt is dissolved in water by stirring, then the saccharide is added. The sample is further stirred until a homogenous mixture is obtained. While sucrose and glucose fully dissolve, cellulose is not soluble in water, but still forms a homogeneous mixture. The samples are directly calcined under nitrogen with a heating ramp of 10 K/min up to 800 °C unless otherwise noted, then cooled down still under nitrogen flow. As a last step the obtained black solid samples are carefully crushed in a mortar. The reaction conditions are summarized in Table 3 with ratio *R* being the carbon to metal ratio.

Table 3: Summary of the reaction conditions for the saccharide route.

Compound	Precursor 1	Precursor 2	C-Source	R (C/M)	Heating
$Pd_{0.9}Ni_{0.1}$	$Pd(NO_3)_2{\cdot}xH_2O$	$Ni(NO_3){\cdot}6H_2O$	Cellulose	33	700 °C [10 K/min]
$Mn_{0.75}Fe_{2.25}C$	$MnAc_2{\cdot}4H_2O$	$FeAc_2$	Cellulose	33	1000 °C [10 K/min]
$Fe_{0.5}Ni_{0.5}$	$Fe(NO_3)_3{\cdot}9H_2O$	$Ni(NO_3){\cdot}6H_2O$	Cellulose	33	900 °C [10 K/min]
$Pd_{0.5}Ni_{0.5}$	$PdCl_2$	$Ni(NO_3){\cdot}6H_2O$	Cellulose	33	800 °C [10 K/min]
Ni	$Ni(NO_3){\cdot}6H_2O$	-	Cellulose	33 16 8	800 °C [10 K/min]
Ni	$Ni(NO_3){\cdot}6H_2O$	-	Sucrose	33 16 8	800 °C [10 K/min]
Ni	$Ni(NO_3){\cdot}6H_2O$	-	Glucose	33 16 8	800 °C [10 K/min]
$Cu_{0.5}Ni_{0.5}$	$CuCl_2{\cdot}2H_2O$	$Ni(NO_3){\cdot}6H_2O$	Glucose	16	800 °C [10 K/min]
$W_{0.15}Ni_{0.85}$	$(NH_4)_6H_2W_{12}O_{40}{\cdot}xH_2O$	$Ni(NO_3){\cdot}6H_2O$	Glucose	16	800 °C [10 K/min]

The scalability of the synthetic pathway was successfully tested up to several grams. The properties and catalytic behavior of the prepared nano-composites will be discussed in chapter 5.

4. Battery Application (Test)

Lithium-ion-batteries, one of the most common rechargeable batteries, are usually applied in portable electronic devices like laptops or mobile telephones. For the improvement of battery systems there are some desired characteristics materials must possess. Since electronic devices request high performances in a very small space, the material should be light with a high energy density. Furthermore, since batteries are used by everyone in daily life the material should ideally be nontoxic.

While lithium brings the advantages of a high electrode potential, lightness and a high energy density used in the cathode material ($LiCoO_2$), graphite is often used as the anode. The carbon host is reduced during the formation of graphite-lithium intercalation compounds, such as LiC_6 among others. The discharging process can be described as in equation (6), while the reaction during the charging of the battery can be described as in equation (7).

$$LiC_6 \rightarrow 6C + Li^+ + e^- \quad (6)$$

$$LiCoO_2 \rightarrow CoO_2 + Li^+ + e^- \quad (7)$$

During the charging process, lithium is extracted from the lattice, but only parts of the lithium can be reversibly extracted.[41]

In order to get improved battery systems it is always needed to have a higher energy density. One way to improve the density is a higher capacity. Another way is a higher difference in the potential between anode and cathode and therefore a small electromotive force and hence a small free enthalpy of the anode reaction is needed. Because the reactions between transition metal oxides or nitrides with lithium are offering a low free enthalpy they could be an attractive anode material.[39] Nowadays, regarding the high performance and large amount of mobile devices used, the charging process is one of the main problems. A high cyclic stability is needed since a conversion reaction is followed by a structural change of the electrode material.[39]

In conversion-type batteries, lithium reacts with a transition metal compound M_mX_n into a two phase nano-composite consisting of the elemental metal and the lithium compound Li_yX. The reaction is indicated in equation (8).[15, 39]

$$M_mX_n + (n \cdot y)\ Li^+ + (n \cdot y)e^- \ \rightleftarrows \ mM^0 + n\ Li_yX \quad (8)$$

Particles in the nano-scale provide short diffusion lengths which could lead to a fast charging and discharging of the corresponding battery.[42] Adding an agent like conductive carbon, such as graphite, enables an improved transport of the electrons between particles and the current collector. Graphite also possesses a high thermal and chemical stability; hence a graphitic shell can serve as a stabilizing agent for particles. Indeed, the shell prevents the material to get oxidized easily when the particles are exposed to air as already observed in other manganese systems for battery application.[8]

Furthermore, when the particles are completely embedded in carbon, the morphology of the electrode and its associated capacity can be maintained better, since the material itself is not directly affected and the particles cannot agglomerate during charging and discharging.[39]

The theoretical capacity of a material can be calculated according to equation (9) where q_{theor} is the theoretical capacity, n is the number electrons involved in the electrochemical process, F is the Faraday constant and M is the molecular weight of the material.[43]

$$q_{theor} = \frac{n \cdot F}{M} \quad (9)$$

The performance of a battery can be improved by increasing the capacity of the materials used. A further discussion of theoretical capacities will be done in chapter 4.1.

4.1. Manganese nitrides and oxides as battery materials

Regarding their varied properties and the resulting possible applications, manganese nitride systems have been widely studied. The four possible phases of manganese nitride which are ε (Mn_4N), η (Mn_3N_2), θ (MnN) and ζ (Mn_5N_2, Mn_2N and $Mn_2N_{0.86}$) with varying ratios of manganese and nitrogen[44] could be obtained by changing the reaction conditions like the nitrification gas, the temperature or the reaction time.[45],[46] The conditions to get manganese nitrides even as bulk systems are usually vigorous, using high pressure nitrification gas, high temperatures, very long reaction times or microwave synthesis.[47] The

four manganese nitride phases do not only differ in their stoichiometric ratio but also in their electronic and magnetic behavior.[15],[44]

Manganese oxide systems are already known as anode material for lithium ion batteries.[48],[49] The performance could already be improved using core-shell structures of MnO encapsulated in graphite.[8]

The presented synthesis will show a simple approach to receive either single phase $MnN_{0.43}$ or a mixed system of $MnN_{0.43}$ and MnO encapsulated in carbon.

The advantage of manganese nitrides and oxides in battery systems can be estimated when looking at the theoretical capacities calculated according to equation (9). In equation (10) an exemplary calculation is shown for MnO giving a theoretical capacity of 756 $mAhg^{-1}$ which is much higher than the state-of-the art graphite (forming LiC_6) that is widely used as an anode material with a theoretical capacity of 372 $mAhg^{-1}$.

$$q_{theor}(MnO) = \frac{2 \cdot 26.8\ A \cdot h \cdot mol^{-1}}{70.9 \cdot 10^{-3}\ kg \cdot mol^{-1}} = 756.0\ \frac{A \cdot h}{kg} = 756.0 \frac{mA \cdot h}{g} \quad (10)$$

Manganese nitride $MnN_{0.43}$ has got a theoretical capacity of 531 $mAhg^{-1}$, which is still higher than the one of graphite. The high specific capacity makes those materials interesting for their application in batteries.

In fact, manganese nitride is already known to reversibly react with lithium to LiN_3 and Mn^0, which makes the synthesized particles even more interesting for lithium ion batteries since cyclic stability is extremely important for rechargeable batteries.[50]

Within the lithium ion battery, the reaction for manganese nitride $MnN_{0.43}$ can be described as estimated in equation (11).[15]

$$MnN_{0.4} + 1.2\ Li \rightleftarrows Mn + 0.4\ Li_3N \quad (11)$$

The reaction for manganese oxide can be described in a very similar way according to equation (12).[8]

$$MnO + 2Li \rightleftarrows Mn + Li_2O \quad (12)$$

Another advantage of manganese oxides and nitrides in particular is the metal's abundance, low toxicity and the associated small prize. On these grounds a large scale commercial production could be possible.

This chapter will discuss the single phase system manganese nitride $MnN_{0.43}$@C and the mixed phase system $MnN_{0.43}$/MnO@C which includes both – oxide and nitride phases. The presented systems will be characterized and compared before and after the discharge in order to get a deeper insight into the process during the battery test. The discharged samples were originally prepared by Bettina Milke[15], while the particles before discharge are freshly prepared.

4.2. MnN@C nano-composite

4.2.1. Battery test of MnN@C

Here the main goal was to investigate potential changes in the systems during the battery test and not the battery test itself, the process and the results will be discussed just shortly.

The electrodes were prepared by taking 85 wt% of the electrode material ($MnN_{0.43}$ prepared as described in chapter 3.1), 10 wt% carbon black and 5 wt% poly(vinylidene difluoride) [PVDF] binder in N-methyl-2-pyrrolidone [NMP] as a solvent and casting this suspension onto a stainless steel current collector. The electrodes prepared with this *tape-casting* process were then dried at 60 °C for 5 h, before heating them to 120 °C for 12 h. Afterwards, the electrodes were tested in a Swagelok® type cell with an Arbin battery tester (3 V – 0.01 V; current density: 10 mAg^{-1}; 25 °C) against lithium foil as counter electrode. The electrolyte consisted of a 1 M $LiPF_6$ solution in ethylene carbonate and dimethyl carbonate. For all analytical purposes, the nano-composite powder was discharged to 0.01 V without the addition of PVDF or carbon black. Before the analysis it was washed with anhydrous dimethyl carbonate.[15, 38]

The material showed fine cyclic stability over 140 cycles giving a capacity of 230 $mAhg^{-1}$ after the first charge/discharge with coulombic efficiencies close to 100%. Due to the low polarization and the low voltage towards Li/Li^+ it might be an attractive anode material in lithium ion batteries. Nevertheless, the capacity is still noticeably lower than the theoretical capacity of $MnN_{0.43}$.[15],[38-39]

4.2.2. Characterization of MnN@C

The phase attribution was made by XRD investigations shown in Figure 3. The figure contains the XRD patterns of the sample before and after discharge. The well-defined reflections can be attributed to $MnN_{0.43}$, which is shown as a reference pattern in red (ICDD 04-007-2198) and the small peak at 26° matches the (002) lattice of graphitic carbon (ICDD 04-014-0362). There is no obvious change in pattern after the discharge, meaning that the particles seem to be stable and unchanged. The stability is very much needed in order to guarantee a long living electrode with a reliable function and which does not undergo oxidation or other side reactions, which would destroy it.

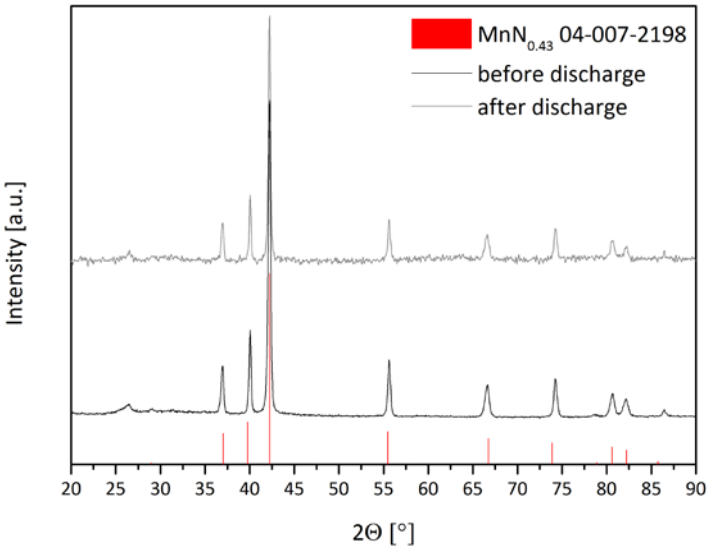

Figure 3: X-ray diffraction of manganese nitride before (a) and after (b) discharge. The peaks can be attributed to $MnN_{0.43}$. Its reference pattern (ICDD 04-007-2198) is shown as red bars.

The results of the elemental analysis for the light elements and of the ICP-OES for manganese, the average size calculated from XRD and obtained from TEM along with the apparent BET surface area are summarized in Table 4.

Table 4: Summary of the experimental results for manganese nitride before and after discharge.

	Elemental analysis [wt%]			Ratio Mn/N	Surface area [m^2g^{-1}]	Average size [nm]	
	C	N	Mn			XRD	TEM
$MnN_{0.43}$ before discharge	27	5.6	68	1:0.324	79.3	27	20 – 50
$MnN_{0.43}$ after discharge	22	3.0	44	1:0.268	not measured	30	40 – 80

It can be seen that there is a change in the chemical composition of the sample during the discharge, being a decrease of manganese, carbon and nitrogen. It is conceivable that the discharged sample is subject to an uptake of oxygen, which does not lead to manganese oxide. The oxygen seems to stay within the carbon matrix, on the surface or is forming amorphous species that are not visible in the XRD. In both composites the ratio between manganese and nitrogen is higher than expected which leads to the assumption, that there are manganese atoms which are differently bonded, for example to carbon.[38] The isotherm of the nitrogen sorption (being a type IV isotherm) can be found in Figure 4 along with the pore size distribution for $MnN_{0.43}$ before the discharge, giving an apparent BET surface area of 79 m^2g^{-1}. The pore size distribution is very broad giving a maximum at 15 and 20 nm, spreading from 12 to 75 nm.

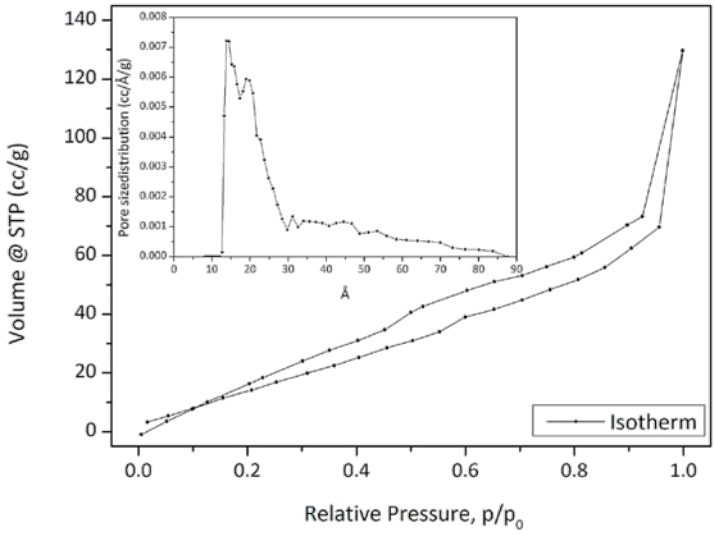

Figure 4: Isotherm of the nitrogen sorption for $MnN_{0.43}$ before discharge. The inset is showing the pore size distribution.

The isotherm exhibits a hysteresis loop as common for type IV isotherms, showing that adsorption and desorption isotherms are different from each other, usually belonging to mesoporous adsorbents.[28] In order to get some insight into the morphology, electron microscopy investigations were performed using SEM, TEM and HR-TEM. The corresponding pictures are shown in Figure 5.

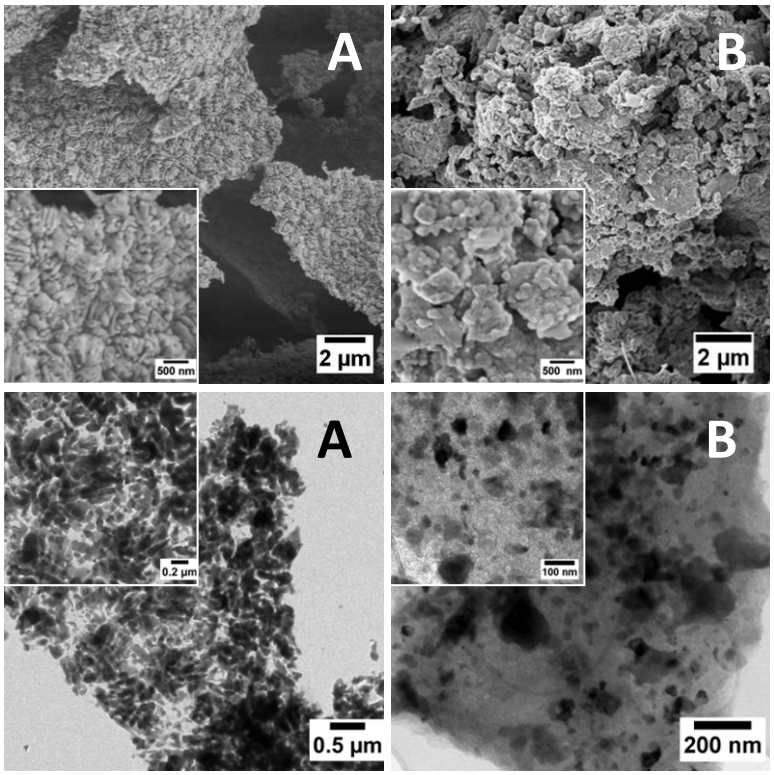

Figure 5: SEM (top) and TEM (bottom) of $MnN_{0.43}$ before (A) and after (B) discharge at different magnifications.

It can be seen clearly that the particle sizes determined by TEM given in Table 4 are a very rough estimation. The particles before discharge are clearly defined, but are rod- or plate-like which are very close to each other, forming larger superstructures.[15] It is even more difficult to estimate a size for the discharged sample. Here the particles seem to be highly agglomerated and are polydisperse in size and shape. The main diffractions of the SAED (selected area electron diffraction) belong to the (002) plane of graphitic carbon, as well as to the (111) and the (300) plane of $MnN_{0.43}$. The diffraction pattern can be seen in Figure 6 along with the indexations for graphite and manganese nitride. Only the most intensive diffraction lines are marked.

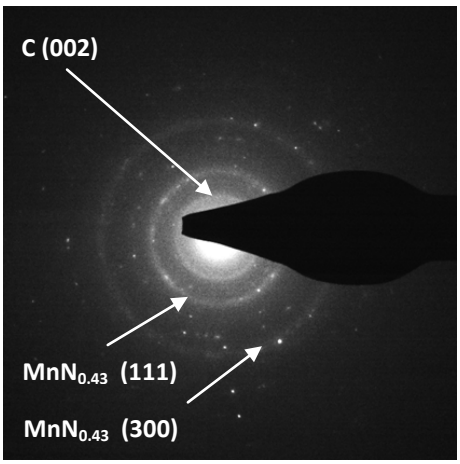

Figure 6: SAED $MnN_{0.43}$ before discharge. Marked are the diffraction data. The reference values for *d* and the *Miller* indices *hkl* were taken from PDF Entry No.: 04-014-0362 (graphite) and 04-007-2198 ($MnN_{0.43}$).

The crystalline nature of the particles could be confirmed by high resolution TEM shown in Figure 7. Additionally, the particles could be identified as core-shell-structures with $MnN_{0.43}$ as the core and graphitic carbon as the shell, as already expected.

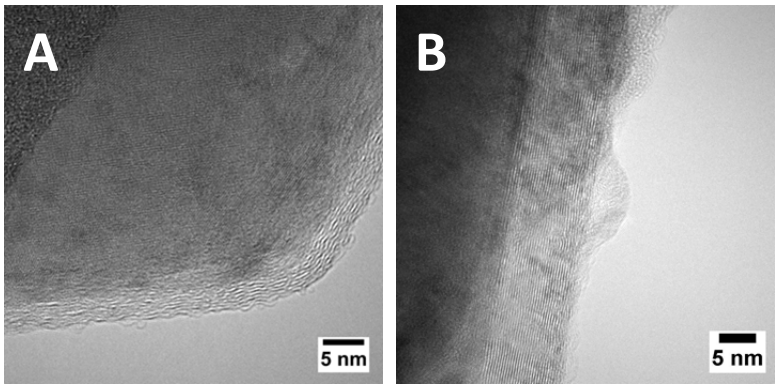

Figure 7: HR-TEM confirms crystalline nature of the particles surrounded by a graphitic shell for the particles before (A) and after (B) discharge.

The crystalline nature of the carbon shell is probably due to catalytic properties of manganese, since manganese and its complexes are known to catalyze the graphitization of carbon. Even at low temperatures it catalyzes the process, which is similar to that of iron.[38],[51] The lattice fringes of the shell belong to graphitic carbon with a distance of d_{exp} = 3.5 Å and d_{exp} = 2.1 Å belonging to the (002) and (101) plane (ICDD 04-014-0362; d_{002} = 3.38 Å and d_{101} = 2.04 Å). The core can be identified as $MnN_{0.43}$ with a distance d_{exp} = 2.2 Å (ICDD 04-007-2198; d_{111} = 2.14 Å). A convenience provided by the carbon shell is the electrical conductivity of graphite, which is important for the application of the particles in electrochemistry and which contributes to the lithium storage capacity. [15],[38],[52],[53] Furthermore, it was shown that the cyclic stability of a conversion type electrode can be greatly enhanced with the encapsulation of particles in a graphitic matrix.[54] The graphitic shell around manganese nitrides synthesized via the urea-glass-route is only up to 10 nm thick, hence the lithium ions can wander through it.[15, 55] In order to further investigate possible changes in the material during the discharge, EELS investigations were used to get a deeper insight into the elemental composition and the chemical bonding in the samples.

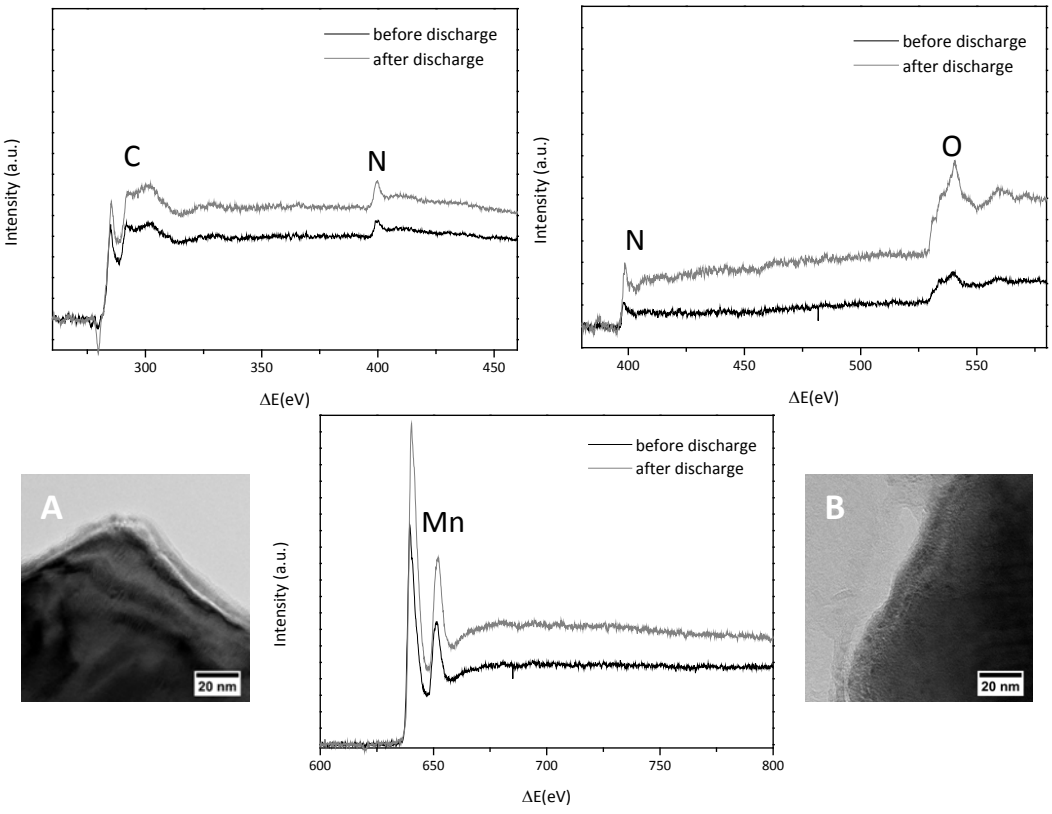

Figure 8: TEM pictures of the selected areas and EELS spectra of manganese nitride before (A) and after (B) discharge.

The TEM pictures from the selected areas and the corresponding EELS spectra are shown in Figure 8. The spectra are showing very similar results for the particles before and after the discharge. The EELS signals taken from the spectra are assigned to the corresponding compounds along with the reference values in Table 5.

Table 5: EELS signals and references for manganese nitride.

Compound	Signal [eV]	Reference [eV]
C (graphite)	285	283.7 - 284.8 [56]
C	288 – 300	
N (nitrides)	399 – 402	≈400 [56]
O in matrix	531 – 535	531 [56]
O	539 – 543	
Mn (nitride)	639.4 – 640.0	639.8 [57]
	650.6 – 652.2	651.0 [57]

The carbon region is showing the specific pattern for graphitic carbon (285 eV). The nitrogen region around 400 eV belongs to nitride compounds. The manganese signal at 640 – 650 eV is common for manganese nitride compounds. Additionally to those peaks which were already expected, there are some signals around 530 – 540 eV belonging to oxygen. The possibility of oxygen within the matrix was already discussed for the discharged sample in the elemental analysis part. Since, according to the elemental analysis of the sample before discharge, it only contains carbon, nitrogen and manganese, there seems to be only a small amount of oxygen. This leads to the assumption, that there might be oxygen on the sample surface, but not necessarily inside the matrix. All in all the presence of manganese nitride could be verified with the signals for manganese and nitride. The small amount of an oxide phase could be associated with a possible passivation layer on the particle surface, since no manganese oxide was found in the XRD or SAED measurements even on the aged or discharged samples.[38] Unexpectedly, in some of the examined areas, some different carbon phases were present (284 – 300 eV), but could not be fully identified apart from the graphitic peak at 284 eV that was constantly present. An exemplary measurement of such an area is shown in Figure 9. Interestingly, the areas with carbon bonded differently did not show any nitrogen content, but rather large oxygen content, hence they do not belong to possible carbodiimide phases. This leads to the assumption, that the oxygen could also be molecularly dissolved in the system, presumably in the carbon matrix.[38]

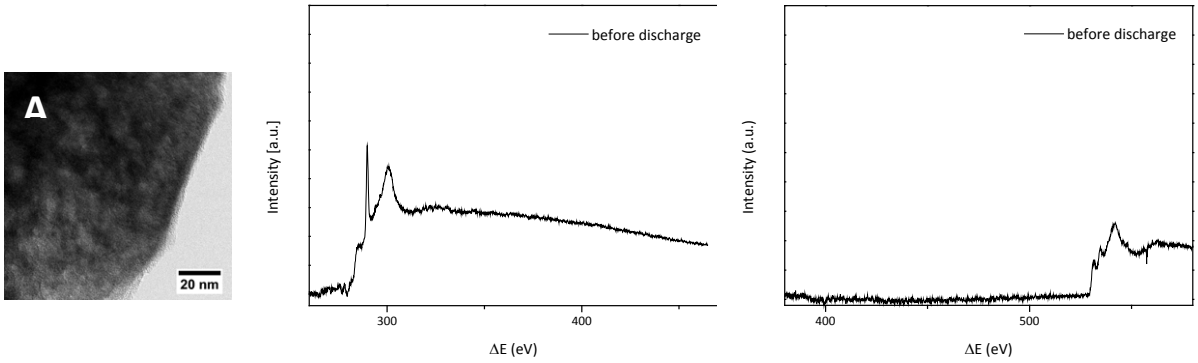

Figure 9: EELS and corresponding TEM image of an area with different carbon phases in $MnN_{0.43}$.

Apart from some unidentified carbon phases, the samples offer some other interesting features. Especially the sample before the discharge contains some particles that diffract a lot in the TEM. Those particles and their corresponding SAED can be seen in Figure 10.

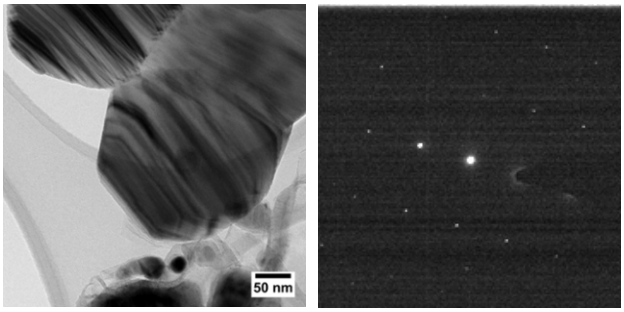

Figure 10: Heavily diffracting $MnN_{0.43}$ particles with the corresponding SAED showing diffraction spots indicating monocrystalline particles.

Those diffracting particles are showing individual spots in the corresponding SAED rather than the usual rings for nanocrystalline particles, indicating their monocrystalline nature. These particles do not show a graphitic shell.

4.3. MnN/MnO@C nano-composite

4.3.1. Battery test of MnN/MnO@C

The electrodes were prepared by mixing 85 wt% of the electrode material ($MnN_{0.43}$/MnO, prepared as described in chapter 3.1), 5 wt% of carbon black and 10 wt% of poly(vinylidene difluoride) [PVDF] binder in N-methyl-2-pyrrolidone [NMP] as a solvent and casting this suspension onto a stainless steel current collector. The electrodes prepared with this *tape-casting* process were then dried at 60 °C for 1 h before heating them to 160 °C for 20 h. Afterwards the electrodes were tested in a Swagelok® type cell with an Arbin battery tester

(0.01 V – 3 V; current density: 10 and 30 mAg^{-1}; 25 °C) against lithium foil as the counter electrode. The electrolyte consisted of a 1 M LiPF6 solution in ethylene carbonate (EC) and dimethyl carbonate (DMC).[39]

For analytical purposes the nano-composite powder was discharged to 0.01 V. Before the analysis it was washed with dimethyl carbonate and dried afterwards.

The material showed fine cyclic stability over 160 cycles giving a capacity of 417 $mAhg^{-1}$ after the first charge/discharge with coulombic efficiencies close to 100%.[39] With the method of *tape-casting* the irreversible loss of capacity during the first cycle can be avoided, giving then a stable specific capacity of 811 $mAhg^{-1}$.[15]

4.3.2. Characterization of MnN/MnO@C

The X-ray diffraction of the sample before and after discharge is shown in Figure 11. The well-defined reflections can be attributed to $MnN_{0.43}$, which is shown as a reference pattern in red (ICDD 04-007-2198) and MnO in blue (ICDD 04-005-4310), while the very small peak at 26° matches the (002) lattice of graphitic carbon (ICDD 04-014-0362).[15] Additionally, there are quite a few supplemental peaks in the spectrum of the sample after discharge. These peaks could be attributed to Li_2CO_3 (ICDD 00-022-1141 in green) which is formed during the preparation of the electrodes. The carbon, in contrast to the route using urea, is in this case mostly amorphous. Interestingly, there is almost no manganese oxide found in the sample after discharge.

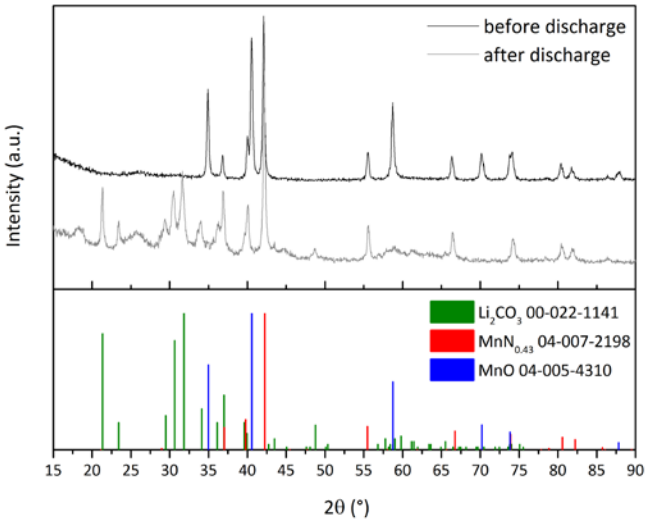

Figure 11: X-ray diffraction of $MnN_{0.43}$/MnO particles before and after discharge. The peaks can be attributed to $MnN_{0.43}$ (red, ICDD 04-007-2198) and MnO (blue, ICDD 04-005-4310). See discussion for additional peaks.

In Table 6 the results of the elemental analysis, the average size calculated from XRD and obtained from TEM along with the apparent BET surface area are summarized. The elemental analysis for the sample after discharge shows a smaller manganese and a higher carbon content. This could be due to the presence of lithium carbonate impurities as already noticed with the XRD. All in all, the carbon content is between 20 and 28 wt% and therefore comparable to the one of single phase $MnN_{0.43}$ prepared using urea as the nitrogen source.

Table 6: Summary of the experimental results for manganese nitride/oxide before and after the discharge.

	Elemental analysis [wt%]			Surface area [m^2g^{-1}]	Average size [nm]	
	C	N	Mn		XRD	TEM
$MnN_{0.43}$/MnO before discharge	20	2.3	67	92.8	26/31	5 – 40
$MnN_{0.43}$/MnO after discharge	28	1.6	40	not measured	26	5 – 40

The apparent BET surface area is higher (92.8 m^2g^{-1}) than the one of $MnN_{0.43}$ as a single phase, which could lead to an increase of available reaction surface. The isotherm of the nitrogen sorption (type IV isotherm) is shown in Figure 12 along with the pore size distribution for $MnN_{0.43}$/MnO before discharge. The pore size distribution is narrowly distributed, much more homogenous than the one of $MnN_{0.43}$ giving a single maximum at 20 nm. The isotherm again exhibits a hysteresis loop as common for type IV isotherms, showing that adsorption and desorption isotherms are different from each other, as already seen for the single phase $MnN_{0.43}$.

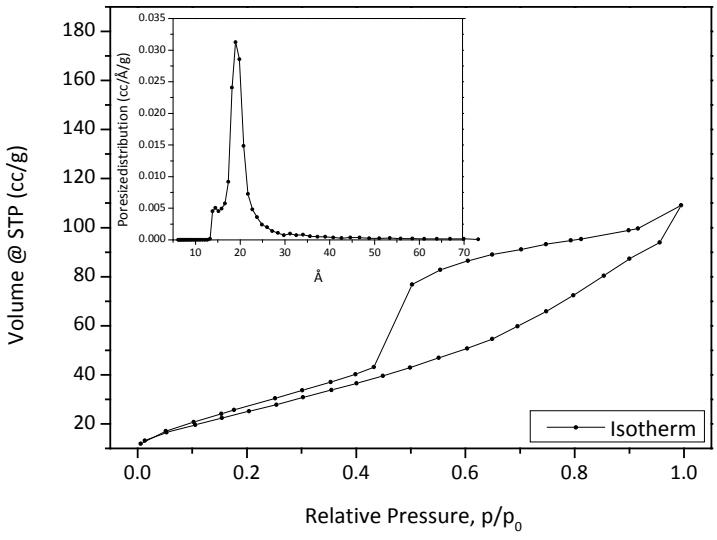

Figure 12: Isotherm of the nitrogen sorption for $MnN_{0.43}$ before discharge. The inset is showing the pore size distribution.

Again, as discovered previously for the simple $MnN_{0.43}$, there is a small change in structure after discharge, but due to the large amount of lithium carbonate within the sample, the chemical composition seems to be changed drastically. The change in the structure of the particles seen in the TEM and SEM is less significant than for $MnN_{0.43}$ alone as it is shown in Figure 13.

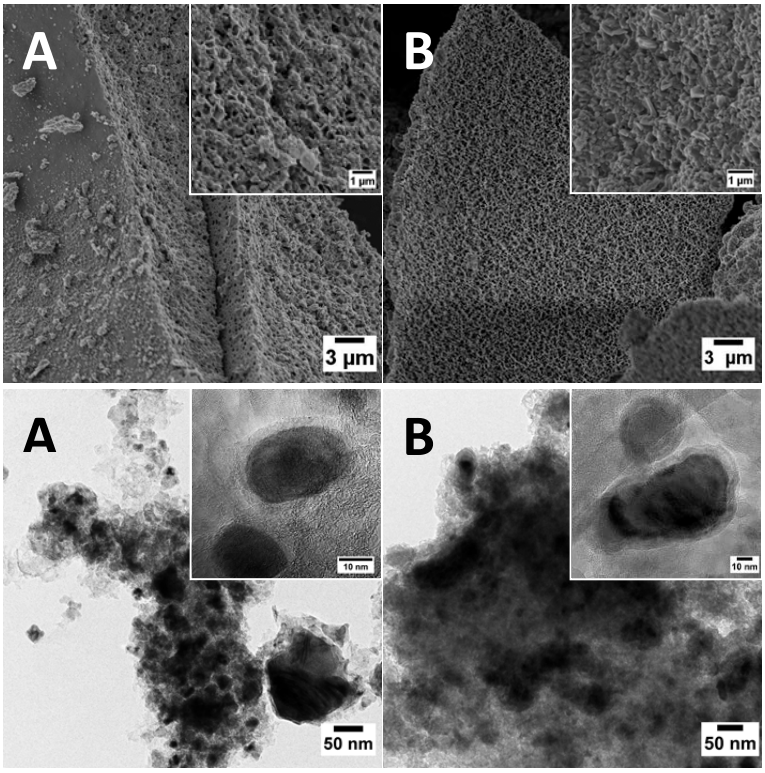

Figure 13: SEM (top) and TEM (bottom) of $MnN_{0.43}$/MnO before (A) and after (B) discharge.

Once more, the particles can be identified as core-shell structures with the shell being carbon and the core being manganese nitride and oxide. In most cases a mixture of nitride and oxide can be found in HR-TEM (Figure 14) and the corresponding SAED (Figure 15). In the sample after discharge the amount of manganese oxide is drastically reduced. The lattice fringes of the shell belong to carbon with a distance of d_{exp} = 3.5 Å and d_{exp} = 2.1 Å, belonging to the (002) and (101) plane (ICDD 04-014-0362; d_{002} = 3.38 Å and d_{101} = 2.04 Å). The core can be identified as $MnN_{0.43}$ with a distance d_{exp} = 2.2 Å (ICDD 04-007-2198; d_{111} = 2.14 Å) and MnO with a distance of d_{exp} = 2.6 Å, d_{exp} = 2.4 Å and d_{exp} = 1.5 Å belonging to the (111), (200) and (220) plane (ICDD 04-005-4310, d_{111} = 2.57 Å, d_{200}= 2.22 Å and d_{220} = 1.57 Å).

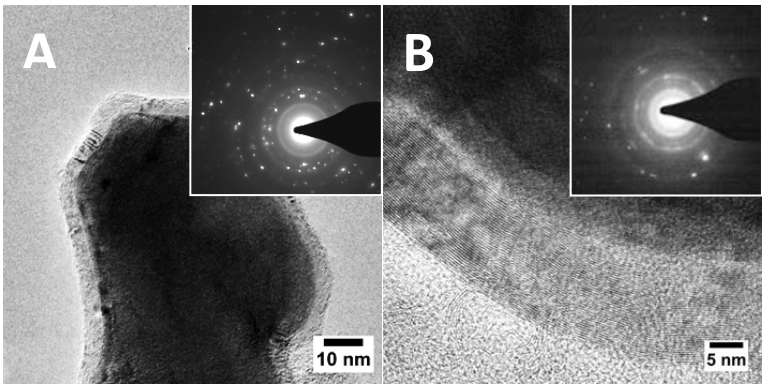

Figure 14: HR-TEM of $MnN_{0.43}$/MnO before (A) and after (B) discharge. The corresponding SAED are shown in the inset.

Due to the two components of the particles, there are plenty of diffraction peaks to be found and assigned in the SAED in Figure 15. The Miller indices in white belong to MnO; the ones in light grey belong to $MnN_{0.43}$. The particles are not monocrystalline, but rather form clusters of smaller particles. While no graphite is observed in the XRD, the carbon shell in the TEM appears rather crystalline; it is therefore presumed to be turbostratic carbon.

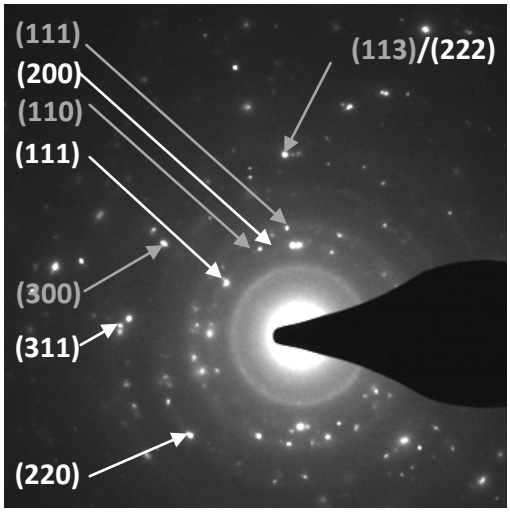

Figure 15: SAED of the $MnN_{0.43}$/MnO nano-composite before discharge and the assigned crystal lattices for MnO (white) and $MnN_{0.43}$ (grey). Only the most intense signals are marked.

Although the majority of particles are a mixture of oxide and nitride before the discharge, a small number of particles can be identified as single phase manganese oxide particles with no signals for manganese nitride as seen in Figure 16.

On the other hand the majority of the particles after the discharge are manganese nitride.

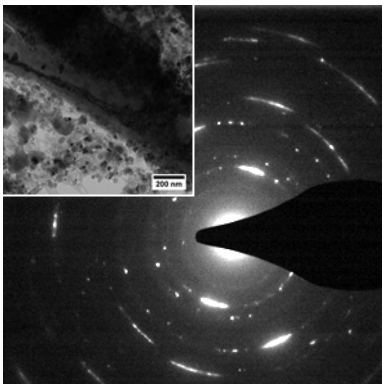

Figure 16: SAED of a single phase MnO particles and the corresponding TEM picture.

The Raman spectra in Figure 17 are showing two main peaks at 1320 cm^{-1} (D band, disorder induced) typical for disordered, amorphous carbon and 1590 cm^{-1} (G band, stretching E_{2g}) typical for graphitic carbon.[58],[59]

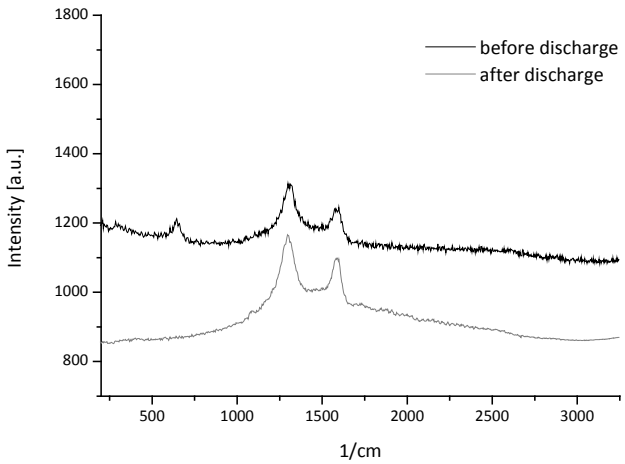

Figure 17: Raman spectra of $MnN_{0.43}$/MnO before and after discharge.

The G band is Raman active for sp^2-carbon networks and indicates the presence of crystalline graphite, while the D band demonstrates the presence of some carbon atoms with a different bonding energy.[60] The band at 640 cm^{-1} can be tentatively attributed to MnO.[61] This would again confirm the loss of manganese oxide during the discharge. As a matter of fact, the loss of manganese oxide during the process of discharge is unexpected since the stability of manganese nitride is supposed to be lower than the one of the oxide. The difference in the theoretical stability and the difference in decomposition temperatures lays in the difference of the bonding energies of N_2 (941 kJ/mol) and O_2 (499 kJ/mol).[62] The reason for the unexpected behavior observed in the system investigated here, could be caused by the process of discharge itself, which should therefore be further investigated in the future.

At first, using urea as a nitrogen source, single phase $MnN_{0.43}$ nanoparticles surrounded by a graphitic shell and embedded in carbon[15] with a high surface area (79 m^2g^{-1}) were synthesized. Although the material showed no remarkable difference in its chemical composition, the particles showed agglomeration after the discharge, but were still stable. A fine cyclic stability of 230 $mAhg^{-1}$ after the first charge/discharge and coulombic efficiencies close to 100% for over 140 cycles were achieved.[15] Due to the graphitic shell, which contributes to the material's resistance, the low polarization and voltage towards Li/Li^+, manganese nitride $MnN_{0.43}$ might be an attractive electrode material for lithium ion batteries. Nevertheless, the theoretical capacity for $MnN_{0.43}$ is remarkably higher than the value reached in the battery test.

An improvement of the cyclic stability to over 160 cycles giving a capacity of 811 $mAhg^{-1}$ could be achieved using a $MnN_{0.43}$/MnO nano-composite embedded in carbon[15] with a surface area of 93 m^2g^{-1} by using guanidine acetate as the nitrogen source. This capacity is noticeably higher than the one of the conventional anode material graphite and even higher than the theoretical capacity of $MnN_{0.43}$ or MnO alone, which makes the mixed nano-composite very interesting. Furthermore, the mixed phase nano-composite is showing a smaller tendency to agglomerate than the single phase system. Unexpectedly, even though the capacity is much higher than of the single phase nitride, the mixed nano-composite seems to lose its oxide phase with only $MnN_{0.43}$ left after the discharge. In order to further investigate the system, oxygen elemental analysis, EELS investigations and atomic mapping will be carried out, as well as a research concerning the mechanism. A major topic will also be the difference between the manganese nitride remaining after discharge of the mixed phase nano-composite, which gives a high capacity of 811 $mAhg^{-1}$ compared to the single phase system, which only gives a capacity of 230 $mAhg^{-1}$. Additionally, single phase MnO will be prepared under argon atmosphere to compare the capacities and the mechanism of discharge.

5. Catalysis with Metal(0) Nanoparticles and Alloys

In this thesis, a variety of ternary transition metal carbides, elemental metal and metal alloy nanoparticles dispersed in a carbon network, synthesized using the saccharide route described in chapter 3.2, are reported. The preparation of nanoparticles embedded in a carbon matrix using cellulose as the carbon source was already described before.[13] Modifications were done towards other carbon sources as sucrose, glucose and lignin, but also towards an improvement of the metal to carbon ratio.

The ultimate target of all catalytic tests is intended to be lignin, the world's second most abundant natural polymer, which is a substantial component of wood. As a result of its not uniform and very complex structure, including very strong bonds that are difficult to cleave, selective catalysts are needed to convert lignin into convenient products.[63] The most difficult part is to isolate lignin and to modify and cleave bonds separately.

Metal nanoparticle systems have been used for several kinds of catalytic reactions. Those systems however had some drawbacks since they were not stable, often involved the use of noble metals, had to be prepared *in situ* or the reactions (catalytic reaction as well as the catalyst preparation) had to be carried out under harsh conditions or using various steps.[10],[11]

Ideally, catalysts should be able to selectively catalyze reactions (like reductions) under mild conditions using low amounts of precious metals. In this thesis potential catalyst systems are prepared, characterized and preliminary catalysis tests carried out. The as prepared catalysts are easy to handle and prepare and are also stable under air, thanks to their carbon embedding.

Before the synthesized catalysts will be tested on lignin itself, some model reactions were used in order to find out which nano-composite is more promising for further tests. With this approach the selectivity of the catalysts can be tested. These systems are models to test the overall catalytic activity for the systems. Some of the catalysts were tested on their ability to catalyze several types of reactions, including alkylation, hydrogenation and transfer hydrogenation. A summary of the investigated reactions is shown in Figure 18.

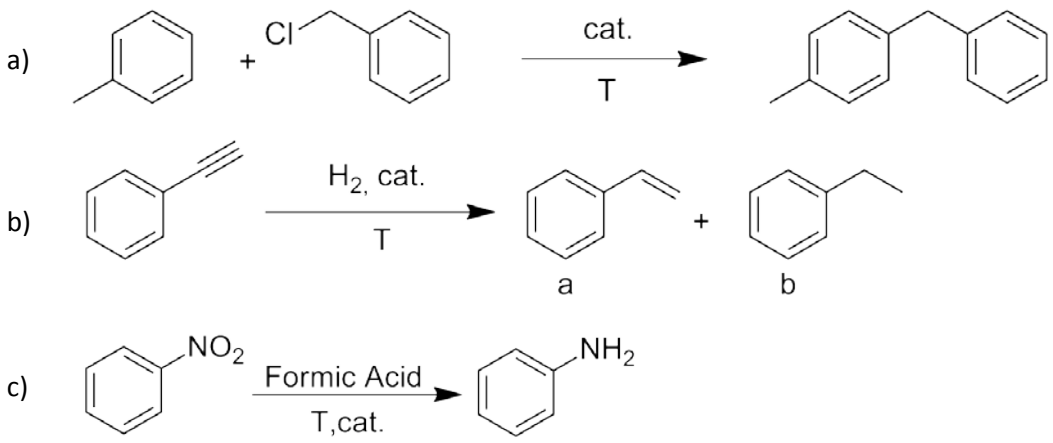

Figure 18: Model reactions to test catalytic properties of the synthesized nano-composites.

5.1. Materials prepared with Cellulose as Carbon Source

The classical saccharide route uses cellulose as the carbon source to build the nano-composite.[13] Basically, it is the purpose of the saccharide to control the morphology of the final products and to provide carbon to form metal carbides. The reason for the use of cellulose in the first place, in contrast to other polysaccharides like starch, can be found in the concept of green chemistry. Animals, including humans, possess an enzyme to cleave the α-1,4-glycosidic linkage between the monosaccharide units of glucose that are contained in starch, but none for the β-linkage in cellulose. Therefore cellulose cannot be digested and is not an aliment; hence it can be used better in green chemical processes.

The nano-composites $Fe_{0.5}Ni_{0.5}$, $Mn_{0.75}Fe_{2.25}C$, $Pd_{0.9}Ni_{0.1}$ and $Pd_{0.5}Ni_{0.5}$ were prepared as discussed in chapter 3.2 with cellulose (carbon to metal ratio R = 33) as the carbon source using the classical approach. Due to the insolubility of cellulose, it is impossible to stir the system. Therefore, it was only possible to carefully shake the crucible in order to soak the cellulose with the precursor solution, which could lead to inhomogeneity.

Before the nano-composites are tested as catalysts, they are characterized thoroughly. Table 7 is showing a summary of the elemental analysis for carbon and of the ICP-OES for the metals (M_1 and M_2 stand for the first and second metal of the alloy), the average size calculated from XRD and obtained from TEM along with the apparent BET surface area (Type IV isotherm). Elemental analysis for palladium was unavailable. The iron content in the ternary carbide is a bit higher than expected. A high surface area was expected since both, the calcined cellulose (surface area: 272 m^2g^{-1}) and the nanoparticles inside the carbon matrix are influencing it.

Table 7: Summary of the experimental results for the cellulose-based nano-composites (R = 33).

	Elemental analysis [wt%]			Ratio M_1/M_2	Surface area [m^2g^{-1}]	Average size [nm]	
	C	M_1	M_2			XRD	TEM
$Fe_{0.5}Ni_{0.5}$	70	10.3	11.0	0.50 : 0.51	174	26	30 - 90
$Mn_{0.75}Fe_{2.25}C$	73	4.8	17.8	0.75 : 2.74	194	28	25 - 30
$Pd_{0.9}Ni_{0.1}$	53	-	1.2	-	240	9	5 – 8
$Pd_{0.5}Ni_{0.5}$	65	-	15.9	-	313	6	8 – 10

The compounds can further be analyzed by XRD measurements, which are shown in Figure 19. The peak at $2\theta = 26°$, which can be seen in each measurement, belongs to graphitic carbon from the carbon matrix. This peak is visible in particular for $Fe_{0.5}Ni_{0.5}$ and $Mn_{0.75}Fe_{2.25}C$, but not so much for the palladium nickel alloys, which can again be attributed to the catalytic activity of iron to graphitize carbon.[52] The palladium nickel alloys are both showing shoulders accounting of pure metal phases, which could not be fully avoided by changing the reaction parameters.

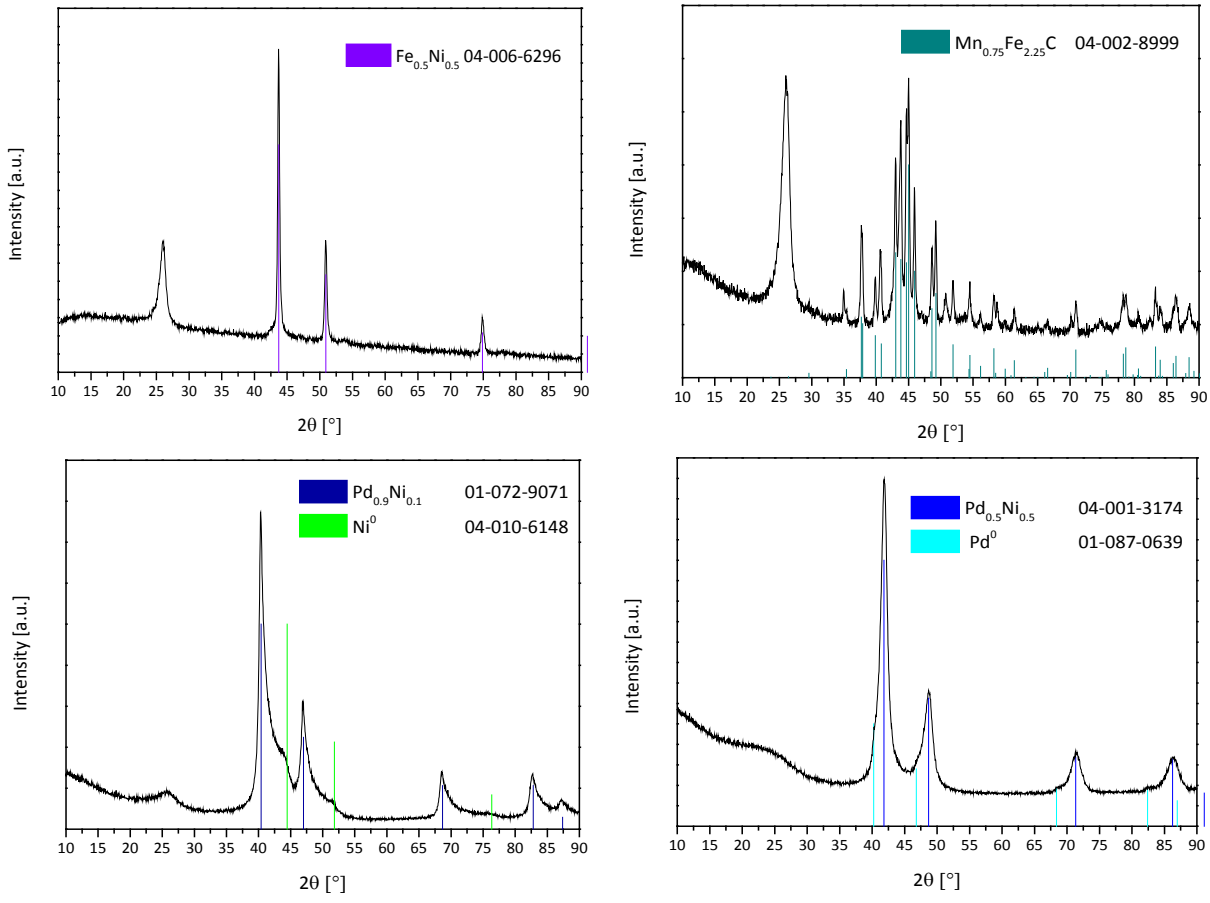

Figure 19: XRD measurements for cellulose-based nano-composites (R = 33).

In order to investigate the systems from a morphology point of view, TEM investigations, shown in Figure 20, were carried out. Since the carbon content is quite high and since the particles are completely embedded in carbon, the TEM grids were prepared by ultramicrotomy.

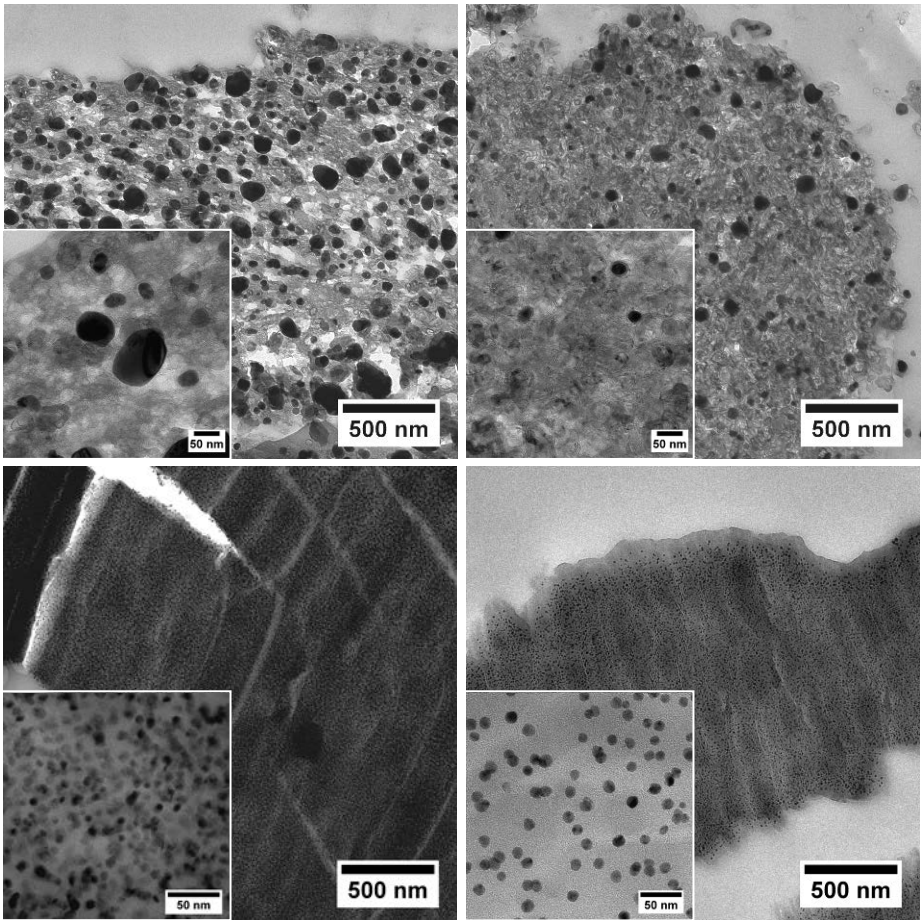

Figure 20: TEM pictures of cellulose-based nano-composites. Top-left: $Fe_{0.5}Ni_{0.5}$, top-right: $Mn_{0.75}Fe_{2.25}C$, bottom-left: $Pd_{0.9}Ni_{0.1}$ and bottom-right: $Pd_{0.5}Ni_{0.5}$.

The change of crystallinity of the carbon can be seen easily as already investigated by XRD. The palladium nickel alloys are showing mostly amorphous carbon while the other two are clearly showing graphitic carbon. Otherwise, the palladium nickel alloys are showing very small, monodisperse, spherical particles. The ternary manganese iron carbide consist of fewer, larger, but still more or less monodisperse particles. The iron nickel alloy on the contrary contains small and very large particles with undefined shape. Further analysis of the sample surfaces was done by SEM, seen in Figure 21.

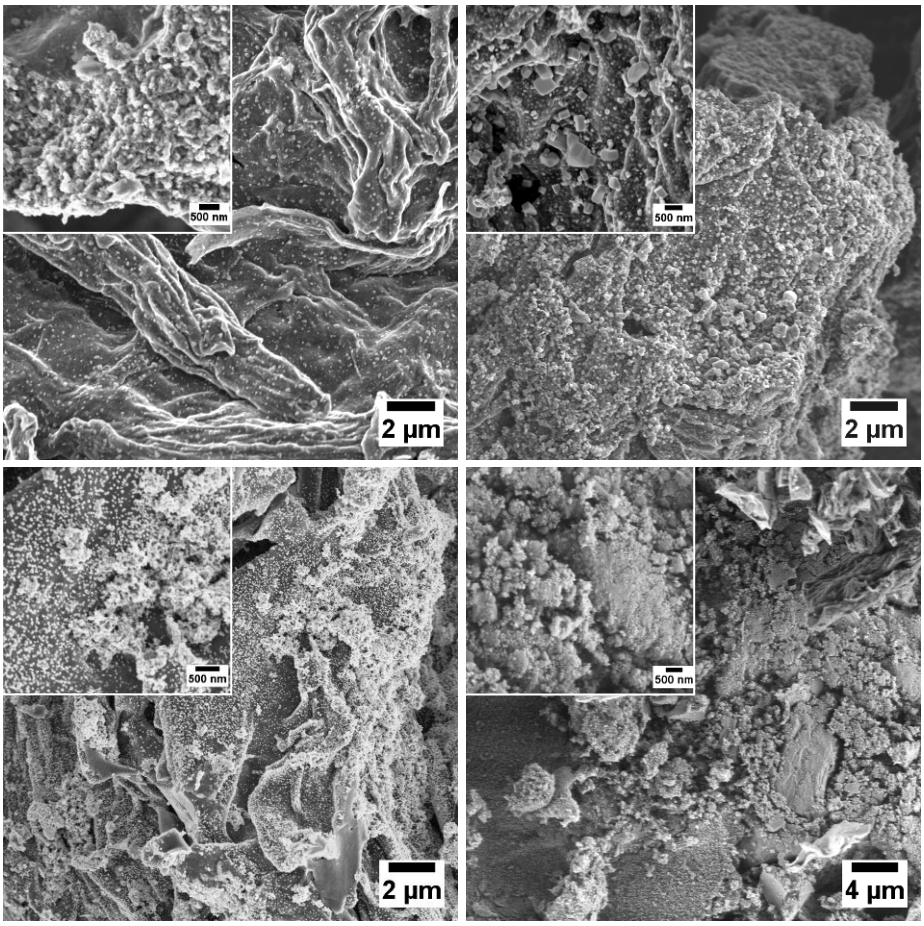

Figure 21: SEM pictures of cellulose-based nano-composites. Top-left: $Fe_{0.5}Ni_{0.5}$, top-right: $Mn_{0.75}Fe_{2.25}C$, bottom-left: $Pd_{0.9}Ni_{0.1}$ and bottom-right: $Pd_{0.5}Ni_{0.5}$.

The SEM pictures clearly show differences between the four systems. While the cellulose structure is kept intact for the $Fe_{0.5}Ni_{0.5}$ with only a few particles to be seen on the surface, the ternary carbide $Mn_{0.75}Fe_{2.25}C$ is forming cubic particles outside of the carbon matrix. The palladium rich alloy is also showing a large amount of uncovered, but spherical particles on the surface. The sample low in palladium does not show any exposed particles, they seem to rather be completely embedded.

The catalytic behavior of the samples could be heavily influenced by the availability of active surfaces. Therefore the ternary carbide $Mn_{0.75}Fe_{2.25}C$ could be a very promising system.

The cellulose-based nano-composites were tested as alkylation catalysts for the reaction of toluene with benzyl chloride towards benzyl toluene. This application of the synthesized and investigated system will be further discussed in chapter 5.4.1.

5.2. Materials prepared with Sucrose/Glucose as Carbon Source

One problem of the cellulose pathway is, since cellulose is not soluble in water and only gets soaked with the precursor solution without the possibility of stirring; the resulting product is never completely homogeneous. Furthermore, the carbon content in the produced samples is always very high. As a result, the particles are usually covered by a graphitic shell and are additionally completely embedded in carbon, which makes the surface hardly available for catalytic applications. In order to solve the mentioned problems, similar carbon sources were used. They were similar in their basic structure of carbohydrates, but the polymeric chain length was shortened. From the polysaccharide cellulose the change was made towards sucrose, a disaccharide composed of two monosaccharide units: glucose and fructose. Sucrose was reported as a possible carbon source for carbon encapsulated nanoparticles before, but the herein presented synthesis is a more facile approach, using less energy (less steps, no vacuum needed, shorter heat treatment, cheaper inert gas).[64] Since sucrose is a food and green chemistry should not use food provisions, the chain length was later further reduced to the monosaccharide glucose.[65] Due to the shorter chain length than in cellulose the two compounds are water soluble and can therefore produce more homogeneous samples.

5.2.1. Nickel^0-System

In order to test the different carbon sources and to improve the reaction conditions, a simple model system was needed to try the different pathways. Since it is a simple, but very promising pathway when it comes to finding a substitute for palladium catalysts, nickel(0) nanoparticles were chosen as a model system. As it will be demonstrated in this section, this system works excellently with the saccharide route showing no side products and reasonably homogeneous particles.

The investigated compounds, synthesized according to chapter 3.2, are the following: *cellulose* (8:1, 16:1, 33:1) as a comparison, *sucrose* (8:1, 16:1, 33:1) and *glucose* (8:1, 16:1, 33:1). The annotation *33:1* signifies the molar ratio between carbon and nickel before calcination being the standard approach.[13] The annotation *16:1* represents half of the standard amount of the carbon source, while *8:1* implies the use of a quarter of the carbon source. These ratios of carbon and nickel in each approach were used to label the samples for all further investigation. The theoretical carbon and nickel content in weight percent was calculated and the values are given in Table 8.

Table 8: Calculated carbon and nickel content in nickel nano-composites.

Ratio C:Ni	8:1	16:1	33:1
C in wt%	63	77	87
Ni in wt%	37	23	13

The carbon and nickel content are calculated assuming that the sample is fully calcined; that is with only nickel and carbon remaining in the samples, without any side products that could contain oxygen or hydrogen. It is only a theoretical value to estimate. The calculated values of the nickel and carbon content can now be compared with the values investigated by elemental analysis, which are shown in Table 9. The hydrogen content in each sample, indifferent to the carbon source, is always around 1 wt% and therefore not significant. It is obvious that the measured carbon content is much lower than the calculated one which is due to the loss of carbon through the formation of carbon dioxide and monoxide during the synthesis. Hence the carbon to nickel ratio is also quite different from the calculated one, the real ratios being approximately 3:1 (*8:1*), 6:1 (*16:1*) and 12:1 (*33:1*).

Table 9: Carbon content in nickel nano-composites investigated by elemental analysis.

	8:1	16:1	33:1
Cellulose	41 wt%	56 wt%	69 wt%
Sucrose	38 wt%	57 wt%	74 wt%
Glucose	37 wt%	57 wt%	71 wt%

Since the carbon content (70 – 75 wt% depending on the metals) of the standard *cellulose 33:1* route was too high, the particles were completely embedded in the carbon matrix. As a result, it was almost impossible to visualize the particles in TEM, which might also lead to difficulties in the accessibility for catalysis.

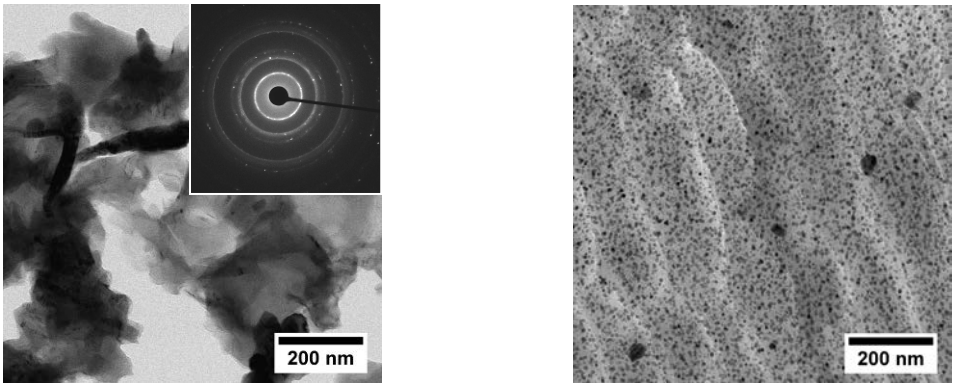

Figure 22: Comparison between TEM samples prepared with the standard method (left) and via ultramicrotomy (right). Both images belong to nickel nano-composites prepared with *sucrose 33:1* as carbon source.

In order to see the particles in TEM, it was necessary to prepare each sample via ultramicrotomy. The same can be stated about *sucrose 33:1* and *glucose 33:1.* The difference between a TEM sample prepared with the standard method and prepared by ultramicrotomy can be seen in Figure 22. If it is not possible to observe the particles without ultramicrotomy preparation, it is nevertheless possible to evidence the presence of the nickel particles by diffraction (see SAED).

Naturally, the decrease of the carbon source amount leads to a decrease of the carbon content in the calcined sample. This results in more exposed particles and an uncomplicated way to prepare the TEM samples. As an overview, the TEM images of the different pathways are shown in Figure 23.

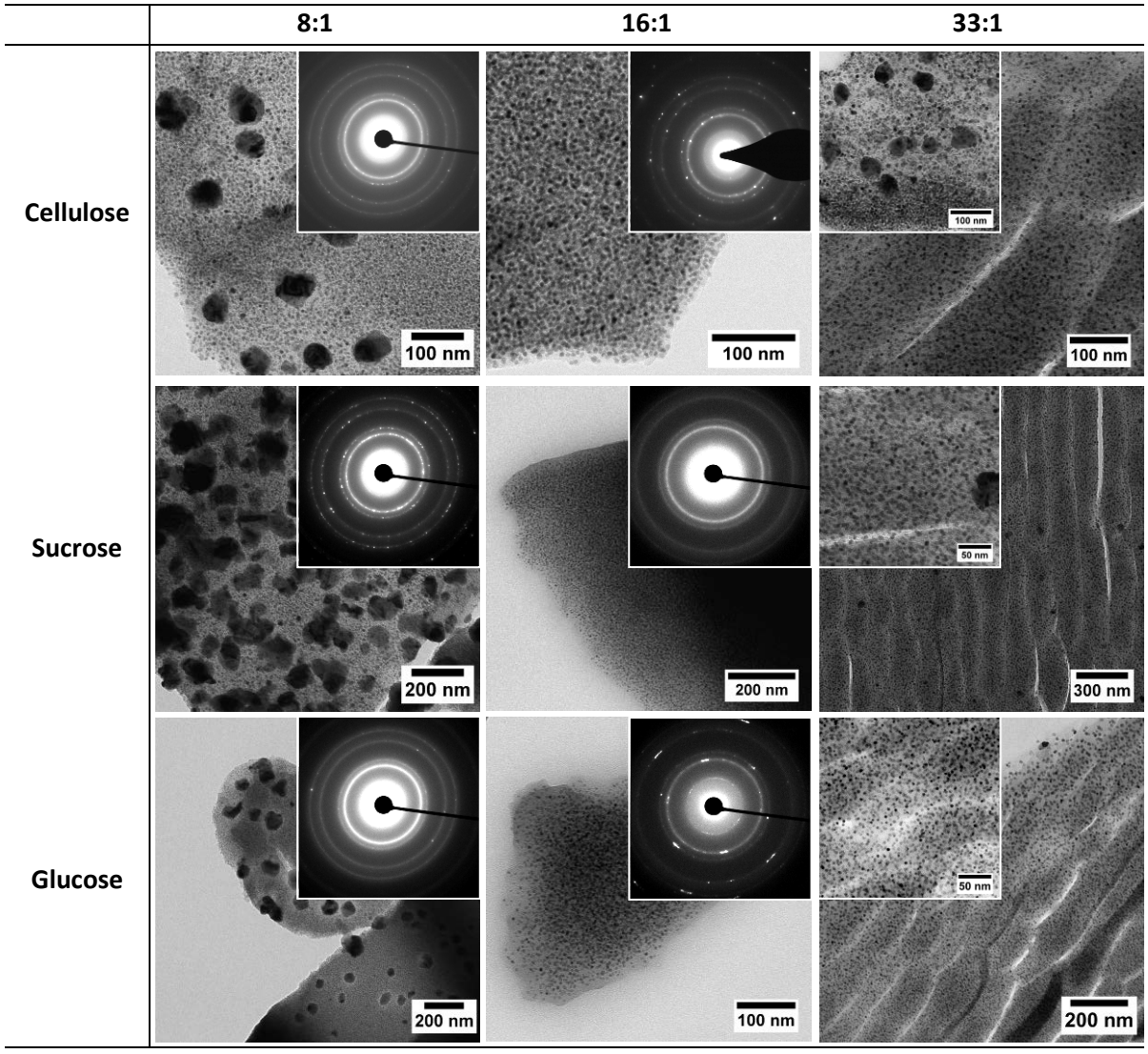

Figure 23: TEM images of nickel nano-composites synthesized using different carbon sources.

The samples with a *33:1* ratio are prepared via ultramicrotomy, the others are prepared by making dispersions in absolute ethanol and depositing two droplets onto a carbon coated copper grid and letting it dry. It has to be pointed out, that the particles in all *16:1* samples are monodisperse with almost no other sized particles to be seen. The *33:1 cellulose* and *sucrose* samples show a large amount of monodisperse, small particles (overview pictures). Nevertheless, they also contain some bigger particles of an undefined shape which are shown in the inset pictures. The *33:1 glucose* sample is also showing monodisperse particles, but in the direction of the carbon edges the particles are getting bigger, ranging from 5 nm particles to 25 nm particles. Possibly, the particles are less stabilized by the carbon matrix on the edges, allowing them to grow to a larger size. In all *8:1* samples small particles are found along with several larger particles of undefined shape.

In every case, the diffraction rings of the SAED correspond to nickel(0) and graphite. The representative indexation is given on the diffraction pattern of *sucrose 8:1* in Figure 24. The graphite is not always visible as in this sample. This is discussed more in the X-ray diffraction part of those samples.

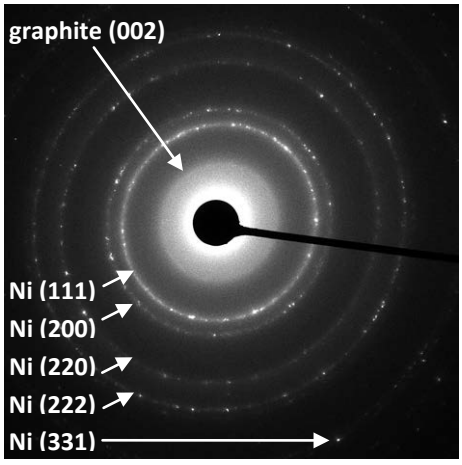

Figure 24: Indexed SAED of Ni^0 prepared with the *8:1 sucrose* approach. The reference values for *d* and the *Miller* indices *hkl* were taken from PDF Entry No.: 04-014-0362 (graphite) and PDF Entry No.: 04-010-6148 (Ni^0).

Further investigation of the nano-composites and their surfaces was done by SEM (pictures in Figure 25). Since the samples already contain a large amount of amorphous and graphitic carbon, they were not sputtered before measuring. The Ni^0 particles in all *33:1* samples are completely embedded in the carbon matrix and cannot be well visualized in the SEM. While the samples with cellulose as carbon source are showing fibers, the glucose and sucrose

samples, very similar to each other, are showing large pieces of carbon with significant edges. These later matrices are forming large bubbles, especially when the carbon content is quite low.

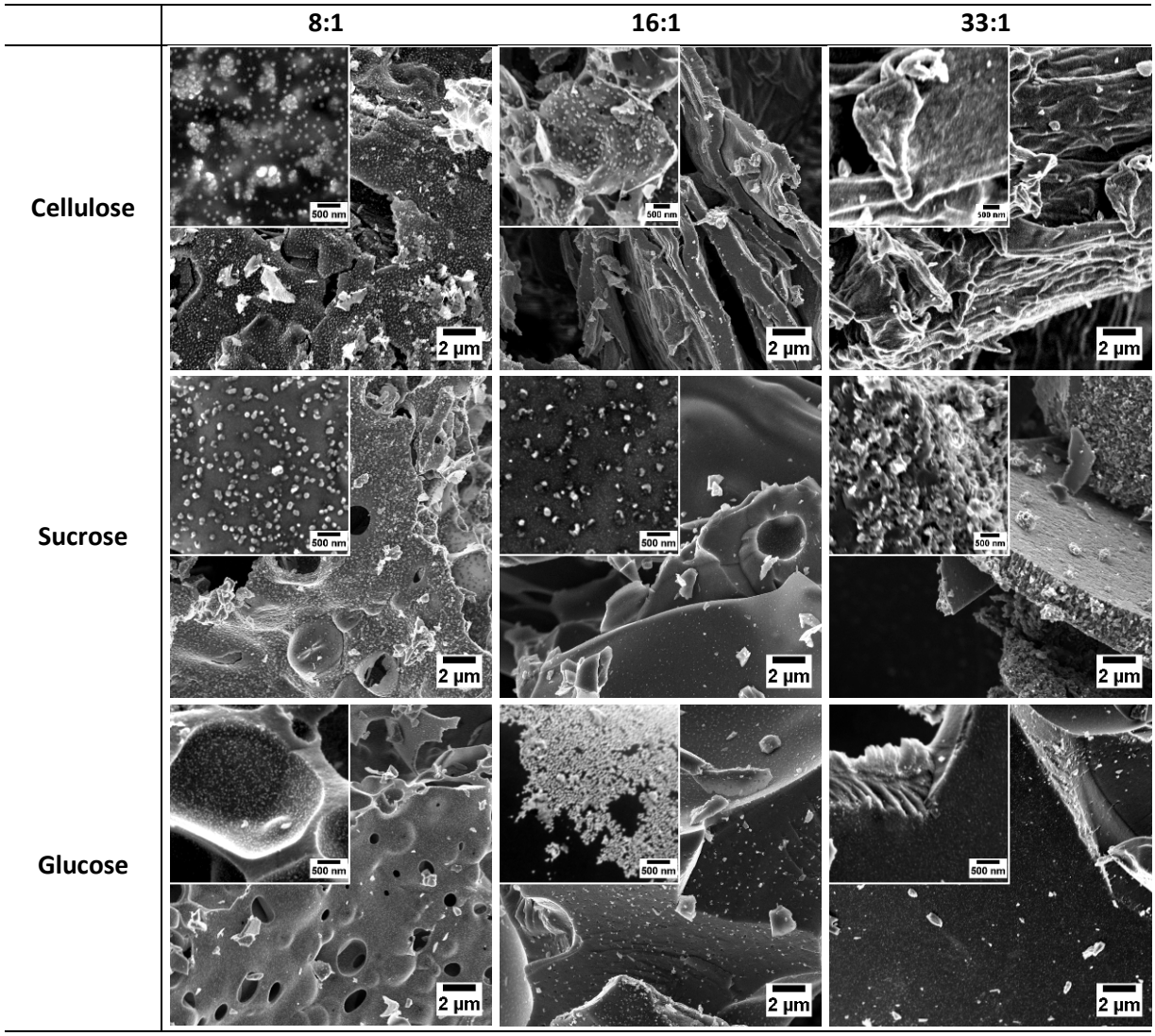

Figure 25: SEM images of nickel nano-composites using different carbon sources.

After looking at the outward appearance of the surfaces, nitrogen sorption measurements were carried out in order to gain statistical information about the surface. While the cellulose-based compounds showed a type IV isotherm, all glucose- and sucrose-based compounds showed a type I isotherm, typical for microporous materials. An exemplary nitrogen sorption isotherm showing this phenomenon is shown in Figure 26.

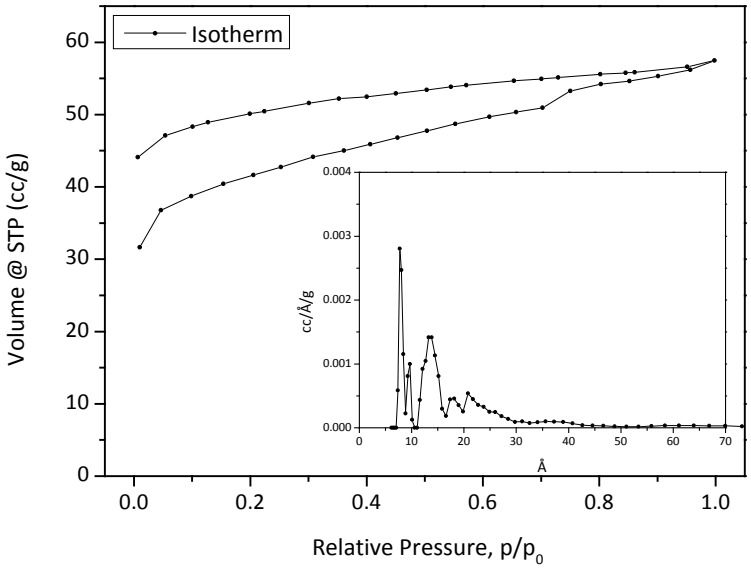

Figure 26: Isotherm of the nitrogen sorption for a sucrose-based nickel^0 nano-composite (R = 8). The pore size distribution is shown in the inset.

A phenomenon that was observed with each of these materials is that the desorption branch does not close to the adsorption branch at low relative pressures, which is often observed for porous polymer networks. An explanation for this behavior is the swelling of the polymer matrix, as well as "pocket filling", where free pores are filled first with the gas, where it does not get desorbed again. The observed phenomenon is still under research.[66] The apparent BET surface areas measured by nitrogen sorption are summarized in Table 10. The surface areas are very high, promising good catalytic activity.

Table 10: Apparent BET surface area of nickel nano-composites using different carbon sources measured by nitrogen sorption.

	8:1	16:1	33:1
Cellulose	168 m^2/g	258 m^2/g	312 m^2/g
Sucrose	145 m^2/g	195 m^2/g	226 m^2/g
Glucose	209 m^2/g	226 m^2/g	346 m^2/g

The nature and structure of the different samples were further studied by XRD measurements. They are displayed in Figure 27. It is obvious from the peak broadening that the sizes of the particles tend to increase with decreasing the amount of carbon. Furthermore, along with the signals for Ni^0 (ICDD 04-10-6148) there is a small peak at $2\theta = 26°$ indicating the presence of graphitic carbon.

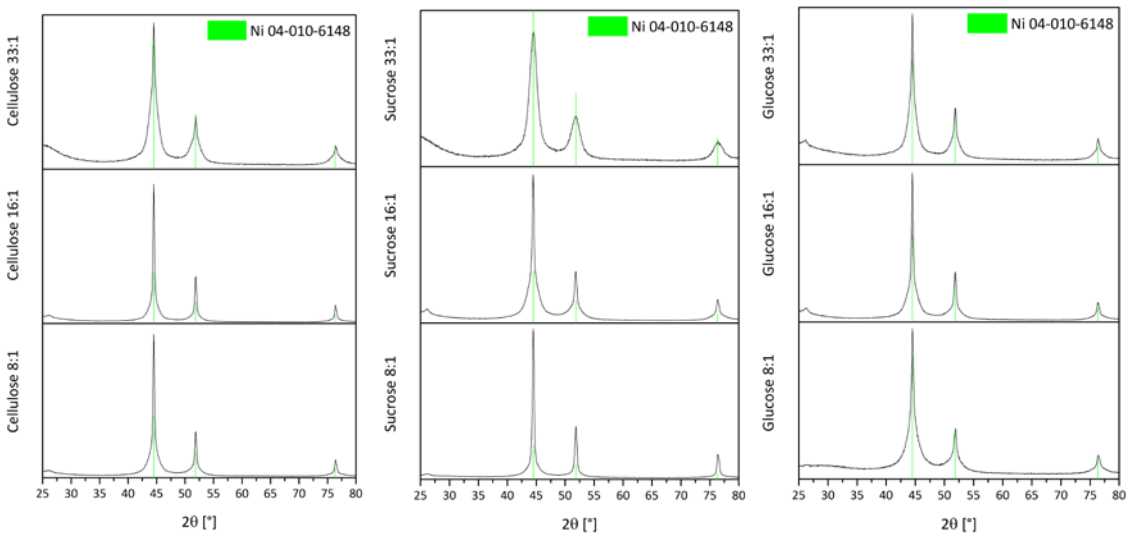

Figure 27: XRD measurements of nickel nano-composites synthesized using different saccharides.

A summary of the particle sizes calculated by XRD and evaluated from TEM data is shown in Table 11. When there is a large amount of other sized particles in the sample, their values are given in brackets. It is obvious that the Scherrer equation is only an indication as it often differs from the values measured by TEM.

Table 11: Sizes of the nickel particles synthesized using different carbon sources and amounts.

	8:1	16:1	33:1
Cellulose	XRD: 25 nm TEM: 3 (50 nm)	XRD: 25 nm TEM: 5 nm	XRD: 11 nm TEM: 5 nm (50 nm)
Sucrose	XRD: 22 nm TEM: 5 nm (100 nm)	XRD: 19 nm TEM: 3 – 10 nm	XRD: 6 nm TEM: 5 – 10 nm
Glucose	XRD: 16 nm TEM: 5 nm (100 nm)	XRD: 20 nm TEM: 3 – 10 nm	XRD: 17 nm TEM: 5 nm

The presence of different particle sizes can already be seen in the XRD measurements since the signals do not follow a Gaussian curve. This is due to the presence of two different size populations in the sample, which give two superposed diffraction patterns: one sharp and intense from large particles and one broad and less intense from small particles.

In conclusion, the synthesis approach could be used for all three carbon sources – cellulose, sucrose and glucose without much influence on the final product. Indeed, the cellulose in which the particles are embedded completely and which is not soluble in water, could be successfully replaced by sucrose and glucose. As a result, the reaction solution can be stirred thoroughly, leading to a homogenous reaction mixture. The objective of this project was to make the particle surfaces easier available for catalysis. It seems that sucrose and glucose are able to fulfill this requirement. Furthermore and for the same objective, the carbon amount was reduced. It was found that using 50% of the saccharide (R = 16) produces monodisperse, small particles that could be easily available. Using 25% of the carbon source on the contrary produces larger particle agglomerates, the system seems less stable. A further advantage of the lower ratio is the avoidable use of ultramicrotomy to prepare TEM samples, which also leads to the assumption that the particles are more exposed and so better accessible for catalysis. As a result, the reaction solution can be stirred thoroughly leading to a homogenous reaction mixture. Since sucrose is an aliment, glucose is the better choice as a carbon source.

5.2.2. Nickel alloys

After modifying the saccharide route towards an ideal carbon to metal ratio (*16:1*), the versatility of the modified approach was tested on different systems to synthesize new nano-composites to be used as catalysts. The synthesis of a copper nickel and tungsten nickel alloy was done according to chapter 3.2 using glucose as a carbon source with a carbon to nickel ratio of 16.

Before the nano-composites are tested as catalysts, they are characterized thoroughly. Table 12 is showing a summary of the elemental analysis for carbon, the average size calculated from XRD and obtained from TEM along with the apparent BET surface area. The surface area of the copper nickel alloy is very high, which also explains the very lightweight nature of the sample.

Table 12: Summary of the experimental results for copper nickel and tungsten nickel nano-composites.

	Elemental analysis [wt%]	**Surface area [m^2g^{-1}]**	**Average size [nm]**	
	C		XRD	TEM
$Cu_{0.5}Ni_{0.5}$	59	353	26 – 30	80 - 300
$W_{0.15}Ni_{0.85}$	48	171	4 – 5	2 – 5; 20 – 50

In order to investigate the structure of the samples, XRD measurements were carried out. These measurements are shown in Figure 28. The copper nickel alloy can be identified as such without any second phase. The synthesis of a pure phase tungsten nickel alloy turned out to be a greater challenge. By using a 1:1 ratio of the two metals, it turned out, according to the XRD measurements, to be a 15:85 ratio alloy of tungsten to nickel with an additional tungsten carbide phase. By trying to initially start the synthesis with this metal ratio, the corresponding alloy was not formed. Instead either nickel(0) and tungsten carbide formed as two separate phases or an alloy with a 7:93 ratio of the two metals was formed with a very small tungsten carbide phase, probably due to small temperature differences within the oven. Nevertheless the sample with the 7:93 ratio, being the one with the least side-products, was further investigated. Since the nominal initial tungsten to nickel ratio is still 15:85 in the sample, this will be the name used for the sample.

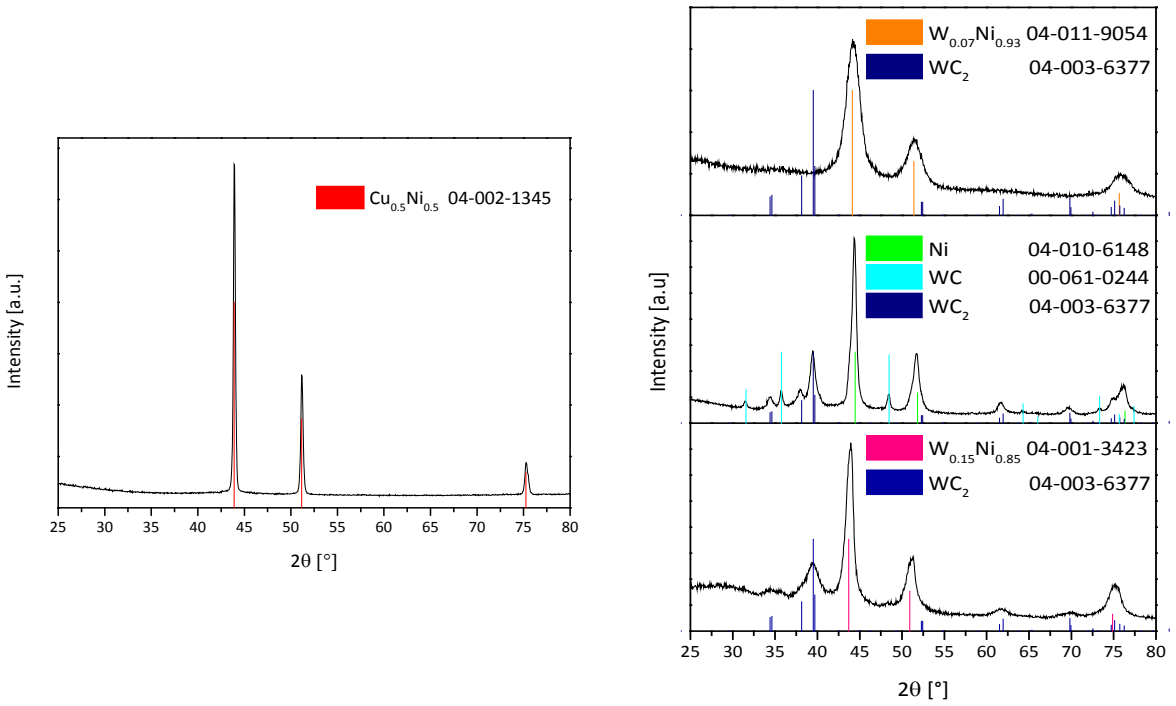

Figure 28: XRD measurements of $Cu_{0.5}Ni_{0.5}$ (left) and $W_{0.15}Ni_{0.85}$ (right, see discussion for details: initial tungsten to nickel ratio of 1:1 (down), 15:85 + slightly higher temperature (middle) and 15:85 + slightly lower temperature (up)) nano-composites prepared with glucose as the carbon source (carbon to metal ratio of 16).

Not only the chemical composition and crystalline structure are interesting to know to understand the catalytic activity, also the particle morphology can be significant. The TEM pictures of the nano-composite alloys are shown in Figure 29. The $Cu_{0.5}Ni_{0.5}$ sample was prepared by ultramicrotomy.

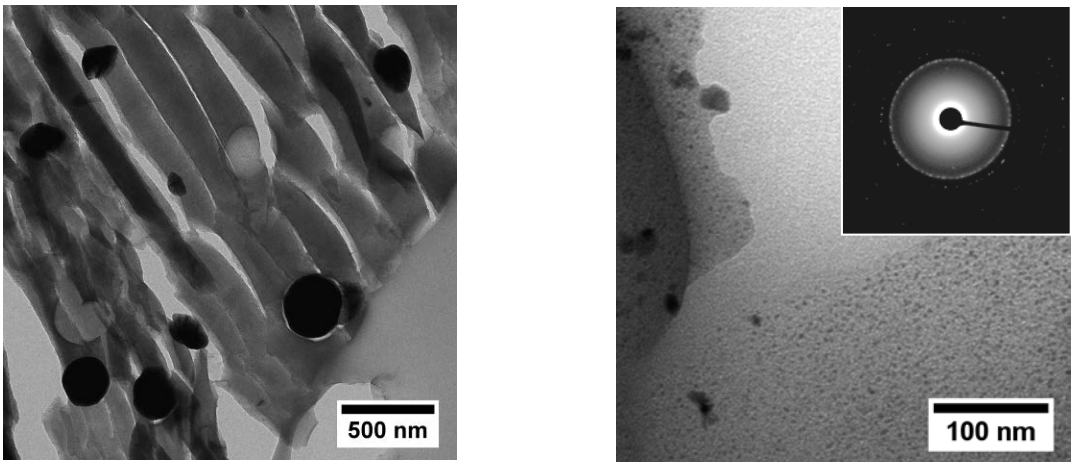

Figure 29: TEM pictures and corresponding SAED measurements of $Cu_{0.5}Ni_{0.5}$ (left) and $W_{0.15}Ni_{0.85}$ (right) nano-composites prepared with glucose as the carbon source (carbon to metal ratio of 16).

The SAED of the tungsten nickel alloy is showing rings corresponding to the (111), (200) and (220) planes of the cubic structure of either nickel or the tungsten nickel alloy. Indeed, it is hard to distinguish between the different alloys and nickel, since they have the same space group with just a very slight difference in the plane distances, differences that cannot be fully distinguished from SAED. The particles of the copper nickel particles are much larger (200 nm) than expected by XRD investigation. The particles seem to be located on the surface, i.e. less embedded in carbon.

Since the surface of the nano-composite is also an interesting feature for catalysis, SEM measurements were carried out. The corresponding images are shown in Figure 30.

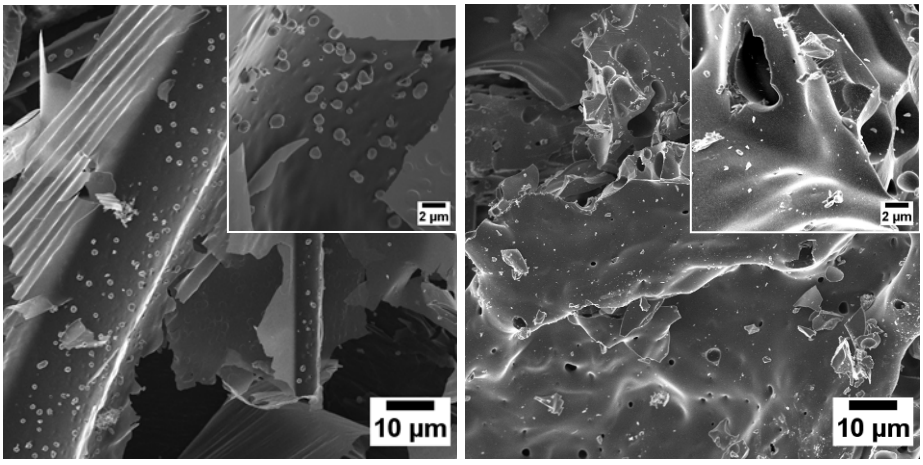

Figure 30: SEM images of $Cu_{0.5}Ni_{0.5}$ (left) and $W_{0.15}Ni_{0.85}$ (right) nano-composites prepared with glucose as the carbon source (carbon to metal ratio of 16).

In both cases the particles seem to be very small and again embedded in carbon. Although both structures are made from the same carbon source, the carbon matrices look very

different from each other. The copper nickel alloy shows some very thin sheets with large particles on the surface, while the tungsten nickel nano-composite seems more compact, which can explain the smaller value of the surface area found by nitrogen sorption.

After all, the tungsten nickel alloy needs some modification of the reaction conditions in order to achieve a single phase alloy. A slightly lower temperature might help to minimize the tungsten carbide side products, but could also lead to the formation of tungsten oxides. Further investigations have to be carried out.

5.3. Materials prepared with Lignin as Carbon Source

After cellulose, sucrose and glucose were all proven to work in a similar way as carbon source, it seemed likely that the method could be used for any (poly)saccharide. Lignin itself, the ultimate target of the catalytic tests, is a polysaccharide network. Therefore it was also tested as a carbon source. This approach is just a first test reaction in order to see if this network performs in a similar way. If so, this would mean a double application of this excess material and therefore less need for energy and chemicals to produce new catalytic systems.

This approach is using some lignin extracted from straw (using alkali conditions, $Ba(OH)_2$ at 250 °C)[67] to test the general ability to apply this material as the carbon source. Again nickel was used as a model system to compare the results with the ones already discussed in chapter 5.2. The synthesis details are summarized in chapter 3.2. Lignin is used as the carbon source with a *33:1* ratio between carbon and metal. The resulting XRD measurements are shown in Figure 31. It can be seen that the synthesis pathway also works for lignin, giving nickel(0) nanoparticles.

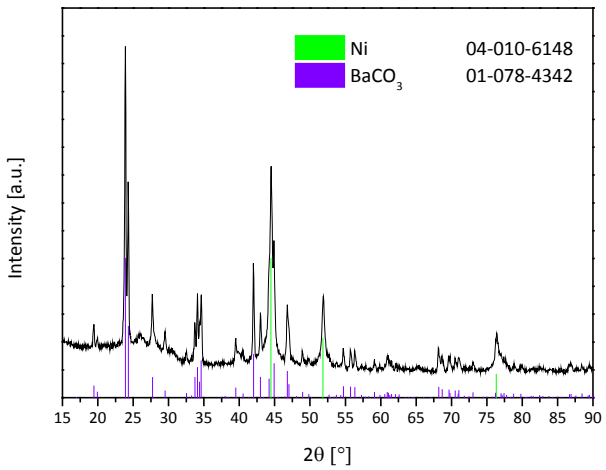

Figure 31: XRD measurement of nickel nano-composite with lignin as carbon source (carbon to nickel ratio of 33).

Apart from the nickel signals, there are other peaks as well. These contamination peaks can be attributed to barium carbonate $BaCO_3$, which is coming from the lignin extraction process. The carbon content investigated by elemental analysis is 54%, while the particle size is estimated to be 20 nm according to the Scherrer equation. SEM measurements were carried out to have an overview of the sample, which is shown in Figure 32. The overall appearance seems to be very similar to the samples obtained with the saccharides used before.

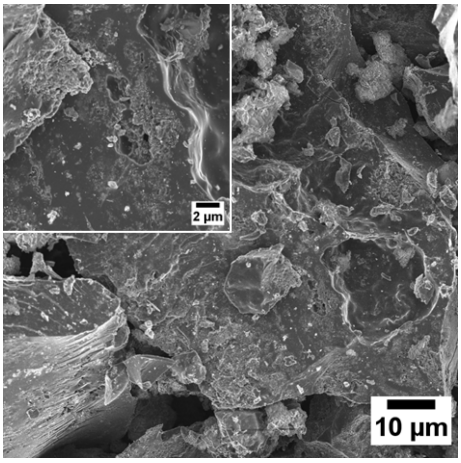

Figure 32: SEM pictures of a nickel nano-composite prepared with lignin as a carbon source (carbon to nickel ratio of 33).

Since the contamination with barium carbonate was really intense, the sample was not analyzed further. Nevertheless, these preliminary results prove that the synthesis pathway also could work with lignin as a carbon source. The only problem that would appear again would be the solubility in water as with cellulose. Using a carbon to nickel ratio of 16 could at least make it possible to stir the reaction mixture before calcination. This pathway should be repeated with ratio of 16 and pure lignin without barium carbonate. This might be achieved by washing away the barium carbonate with HCl.

5.4. Catalysis

5.4.1. Alkylation using $Mn_{0.75}Fe_{2.2.5}C$ as catalyst

The catalytic activity of nano-composites synthesized with the cellulose route was tested in an alkylation reaction of toluene with benzyl chloride to get benzyl toluene by Prof. Dr. Rafael Luque. This model reaction is shown in equation (13).

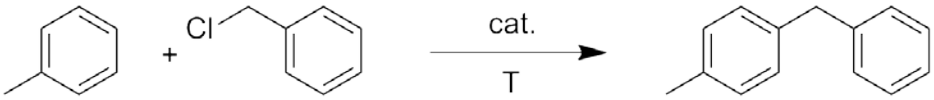

(13)

For this reaction all nano-composites presented in chapter 5.1 were tested as possible catalysts. There was no catalytic activity to be found for this reaction with $Pd_{0.9}Ni_{0.1}$, $Pd_{0.5}Ni_{0.5}$ and $Fe_{0.5}Ni_{0.5}$ as catalysts, nor for similar reactions using benzyl alcohol. Interestingly, the only ternary carbide that was synthesized, $Mn_{0.75}Fe_{2.2.5}C$, was the only system that showed catalytic activity. The reactions were conducted under conventional heating at 110 °C using 4 mL of benzyl chloride, 5 mL of toluene and 100 mg of the tested catalyst. The corresponding results for $Mn_{0.75}Fe_{2.2.5}C$ are shown in Table 13.

Table 13: Results of the catalytic alkylation of toluene with benzyl chloride using $Mn_{0.75}Fe_{2.2.5}C$ as catalyst.

Time	Conversion [%]	Selectivity [%] benzyl toluene		
		meta	ortho	para
15 min	-	-	-	-
30 min	-	-	-	-
45 min	12	8	42	50
60 min	18	9	42	49
90 min	22	8	43	49
120 min	27	9	43	48
150 min	34	8	42	50
180 min	38	7	43	50
4 h	54	7	44	49
5 h	70	6	45	48
6 h	79	6	45	49
8 h	88	6	45	49
9 h	98	6	45	49
24 h (blank run)	5	10	40	50

The proportion of the different isomers is as expected under conventional heating. Without catalyst the reaction only works with 5% of conversion within a reaction time of 24 hours. Adding the ternary carbide nano-composite to the reaction mixture leads to almost full conversion within 9 h.

Additionally to the reaction under conventional heating some preliminary results for an analogous reaction under microwave irradiation were done. Herein a conversion of over 95% within 10 min of reaction time can be observed. The most unusual thing about this microwave reaction is the selectivity of 80% towards the *meta*-product which is not thermodynamically favored. The reason for this unusual behavior could be the high production of energy by carbides under microwave radiation leading to higher temperatures within the reaction vessel.[68] This reaction is under further research but seems to be very promising. Kinetic studies are still under research.

Some preliminary catalytic tests using the catalyst $Mn_{0.75}Fe_{2.25}C$ for the conversion of starch and glucose to valuable furanics were also attained with exceptional results. This reaction is still under further research.

5.4.2. Reduction of triple bonds

Selective triple bond hydrogenation of alkynes is a necessary reaction for industrial processes in both, fine chemical synthesis and bulk productions and is usually carried out using palladium poisoned with sulfate.[69] The model reaction studied here is shown in equation (14). It was already reported before with nickel^0 nanoparticles as catalysts, but those were not stable and had to be prepared *in-situ*.[10] Our as prepared nano-composites are in contrast stable enough and easily prepared in a scalable reaction.

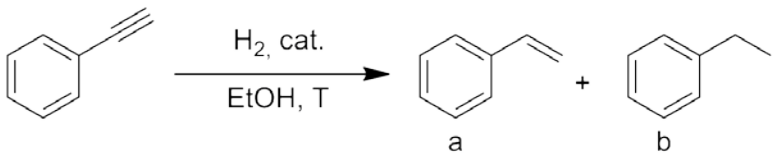

(14)

The reactions were carried out in the H-Cube reactor described in chapter 2.6. The amounts of catalyst used, set by the size of the cartridges are summarized in Table 14 along with the carbon and nickel content. The amount of the copper nickel alloy is a lot lower than the others because this nano-composite is not dense.

Table 14: Summary of the sample details filled into cartridges for the H-Cube reactor.

Catalyst	amount [mg]	Carbon content [wt%]	Nickel content [mmol]
Ni (Sucrose, 16)	686	56	5.2
Ni (Glucose, 16)	630	62	4.1
$Ni_{0.85}W_{0.15}$ (Glucose, 16)	659	48	4.5
$Ni_{0.5}Cu_{0.5}$ (Glucose, 16)	414	60	1.4

The reaction shown above in equation (14) was carried out from a 0.05 M solution of phenylacetylene in ethanol using the H-Cube reactor described in chapter 2.6. The reaction pressure *p* was set to 12 bar, the flow *F* and temperature *T* are shown along with the received substances S (a and b standing for the alkene and the alkane product) and global conversions *X* in Table 15. The focus was set onto nickel nanoparticles using a carbon to nickel ratio of 16 and sucrose as a carbon source first. Later on, after deciding for glucose as a better choice of carbon source, a reaction to compare the catalytic activities was made. Both catalysts seem to perform similarly. The tungsten nickel nano-composite did not perform as well when using a low temperature (≤75 °C), but showed the same catalytic activity at a temperature of 85 °C as the nickel catalysts. The catalytic performance could be even improved by using the copper nickel alloy which already shows full conversion at 75 °C.

Table 15: Results of the catalytic reduction of phenylacetylene using nano-composites prepared by the saccharide route presented in chapter 3.2 as catalysts.

Catalyst	F [mL/min]	T [°C]	X [%]	S [%]	
				a	b
Ni (Sucrose, 16)	0.5	50	7	100	-
Ni (Sucrose, 16)	0.3	50	13	100	-
Ni (Sucrose, 16)	0.3	75	90	90	10
Ni (Sucrose, 16)	0.3	85	100	73	27
Ni (Sucrose, 16)	0.5	85	100	100	-
Ni (Sucrose, 16)	0.3	100	100	60	40
Ni (Sucrose, 16)	0.5	125	100	-	100
Ni (Glucose, 16)	0.5	85	100	100	-
$Ni_{0.85}W_{0.15}$ (Glucose, 16)	0.5	75	76	100	-
$Ni_{0.85}W_{0.15}$ (Glucose, 16)	0.5	85	100	100	-
$Ni_{0.5}Cu_{0.5}$ (Glucose, 16)	0.5	75	100	100	-
$Ni_{0.5}Cu_{0.5}$ (Glucose, 16)	0.5	85	100	74	26

Using Ni (sucrose, 16) it was possible to change from a complete conversion towards the alkene (product *a*), to the complete conversion towards the alkane (product *b*) by increasing the temperature from 85 °C to 125 °C. This temperature difference is low enough to tune the outcome of the reaction towards the desired product, but high enough to have pure compounds even with a slight temperature fluctuation, leading to a reaction that is not too sensitive.

5.4.3. Transfer hydrogenation of nitro groups

Transfer hydrogenation uses an organic molecule as hydrogen donor, in this case formic acid, instead of hydrogen gas. The reduction of nitro groups to the corresponding amines is known to be catalyzed by palladium/platinum-on-carbon or Raney-nickel.[70] The as prepared nano-composites are more stable under air and much easier to handle and prepare; they could therefore be a superior alternative. For this reduction of nitrobenzene to aniline, shown in equation (15), a transfer hydrogenation reaction is used.

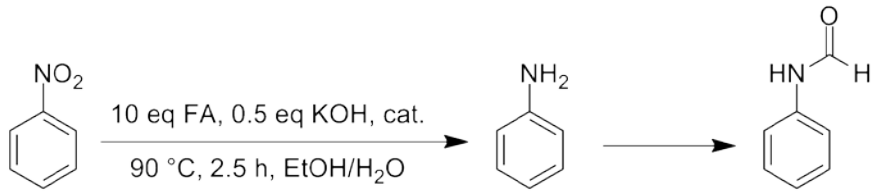

(15)

For this reaction 0.5 eq of the corresponding catalyst (based on the metal content) were put into a pressure tube along with 10 eq of formic acid (FA) and 0.5 eq of KOH in $EtOH/H_2O$ under Argon and stirred for 2.5 h at 90 °C. The nickel nanocomposites, prepared using cellulose, sucrose and lignin (R = 16; 33) as carbon sources, were tested along with two reference compounds being exposed nickel nanoparticles and nickel nanoparticles supported on carbon. The exposed nickel nanoparticles were synthesized by heating a Ni(II) salt to 800 °C under nitrogen flow without any carbon source. Nickel nanoparticles on carbon were prepared similarly to the saccharide route, but in two steps; first the cellulose is pre-calcined alone, then nickel is added from a nickel salt solution and re-calcined. The different pathways are shown in the illustration in Figure 33.

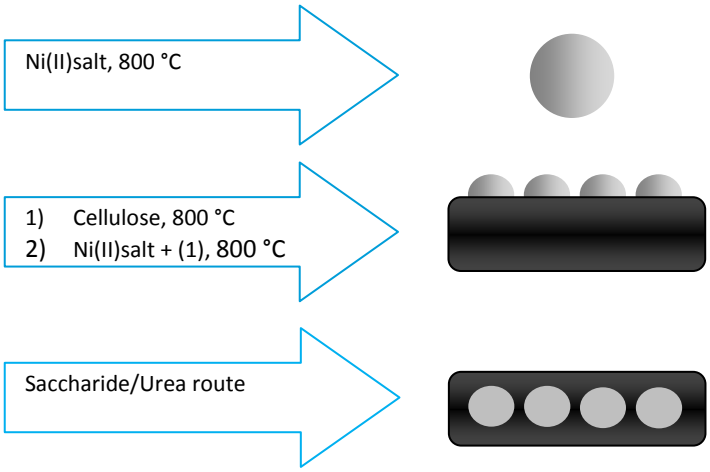

Figure 33: Schematic illustration of different pathways in order to synthesize nickel nanoparticles with different environments.

The results of the catalytic tests are summarized in Table 16. It can clearly be seen that nickel on carbon has the lowest catalytic activity (12% conversion) probably due to the fast oxidation of the small, but exposed nanoparticles. The nude nickel particles are polydisperse and larger since nothing stops their growth during the synthesis but, due to their large amount of directly active surfaces, the conversion is quite high, reaching 68%.

The conversion for nanocomposites prepared with a ratio of 33 are around 50% for all carbon sources, with cellulose having the lowest conversion (47%) and sucrose the highest (56%). Reducing the carbon content to a carbon to nickel ratio of 16, should increase the amount of available nickel surfaces since the nanoparticles are less embedded in carbon. And indeed, the conversion increases; for cellulose this increase only leads to 61% of conversion, while the sucrose shows a conversion of 90%.

Table 16: Results of the catalytic reduction of nitrobenzene using nickel nano-composites as catalysts.

Catalyst	Conversion [%]
Ni (Cellulose, 33)	47
Ni (Sucrose, 33)	56
Ni (Lignin, 33)	52
Ni (Cellulose, 16)	61
Ni (Sucrose, 16)	90
Ni (on C)	12
Ni (exposed)	68

Also the lignin-based nano-composite shows very promising results. After improvement of the purity of the lignin used and reducing the carbon to nickel ratio to 16, the catalytic activity should again be tested thoroughly. The reaction was not tested for glucose yet, similar results to sucrose are expected.

6. Summary and Outlook

It was the goal of this work to explore two different synthesis pathways using green chemistry. The first part of this thesis is focusing on the use of the urea-glass route towards single phase manganese nitride and manganese nitride/oxide nano-composites embedded in carbon, while the second part of the thesis is focusing on the use of the "saccharide route" (namely cellulose, sucrose, glucose and lignin) towards metal (Ni^0), metal alloy ($Pd_{0.9}Ni_{0.1}$, $Pd_{0.5}Ni_{0.5}$, $Fe_{0.5}Ni_{0.5}$, $Cu_{0.5}Ni_{0.5}$ and $W_{0.15}Ni_{0.85}$) and ternary carbide ($Mn_{0.75}Fe_{2.25}C$) nanoparticles embedded in carbon.

In the interest of battery application, $MnN_{0.43}$ nanoparticles surrounded by a graphitic shell and embedded in carbon with a high surface area (79 m^2g^{-1}) were synthesized, following a previously set route.[15] The comparison of the material characteristics before and after the discharge showed no remarkable difference in terms of composition and just slight differences in the morphological point of view, meaning the particles are stable but agglomerate. The graphitic shell is contributing to the resistance of the material and leads to a fine cyclic stability over 140 cycles of 230 $mAhg^{-1}$ after the first charge/discharge and coulombic efficiencies close to 100%. Due to the low voltage towards Li/Li^+ and the low polarization, it might be an attractive anode material for lithium ion batteries. However, the capacity is still noticeably lower than the theoretical value for $MnN_{0.43}$. A mixture of $MnN_{0.43}$ and MnO nanoparticles embedded in carbon (surface area 93 m^2g^{-1}) was able to improve the cyclic stability to over 160 cycles giving a capacity of 811 $mAhg^{-1}$, which is considerably higher than the capacity of the conventional material graphite (372 $mAhg^{-1}$). This nano-composite seems to agglomerate less during the process of discharge. Interestingly, although the capacity is much higher than of the single phase manganese nitride, the nano-composite seems to only contain $MnN_{0.43}$ nanoparticles after the process of discharge with no oxide phase to be found. Future investigations will include EELS investigations and atomic mapping along with a research about the mechanism. Furthermore it will be interesting to see the difference between the manganese nitride remaining after the discharge, which gives a high capacity of 811 $mAhg^{-1}$ and the single phase system, which only gives a capacity of 230 $mAhg^{-1}$.

Concerning catalysis application, different metal, metal alloy, and metal carbide nanoparticles were synthesized using the saccharide route, the ultimate future target of

catalysis being lignin. At first, systems that were already investigated before,[13] being $Pd_{0.9}Ni_{0.1}$, $Pd_{0.5}Ni_{0.5}$, $Fe_{0.5}Ni_{0.5}$ and $Mn_{0.75}Fe_{2.25}C$ using cellulose as the carbon source were prepared and tested in an alkylation reaction of toluene with benzylchloride. Unexpectedly, the metal alloys did not show any catalytic activity, but the ternary carbide $Mn_{0.75}Fe_{2.25}C$ showed fine catalytic activity of 98% conversion after 9 hour reaction time (110 °C).

In a second step, the saccharide route was modified towards other carbon sources and carbon to metal ratios in order to improve the homogeneity of the samples and accessibility of the particle surfaces. The used carbon sources sucrose and glucose are similar in their basic structure of carbohydrates, but reducing the (polymeric) chain length. Indeed, the cellulose could be successfully replaced by sucrose and glucose. A lower carbon to metal ratio was found to influence the size, homogeneity and accessibility (as evidenced by TEM) of the samples. Since sucrose is an aliment, glucose is the better choice as a carbon source.

Using glucose, the synthesis of $Cu_{0.5}Ni_{0.5}$ and $W_{0.15}Ni_{0.85}$ nano-composites was also possible, although the later was never obtained as pure phase. These alloy nano-composites were tested, along with $nickel^0$ nanoparticles also prepared with glucose and on their catalytic activity towards the reduction of phenylacetylene.

The results obtained let believe that any (poly) saccharide, including lignin, could be used as carbon source. In case of lignin, we can also obtain metal nano-composites, although a large contamination of barium carbonate (due to the extraction process of lignin) was observed, which could be avoided by washing the lignin with hydrochloric acid ahead. The $nickel^0$ nano-composites prepared with lignin as a carbon source were tested along with those prepared with cellulose and sucrose for their catalytic activity in the transfer hydrogenation of nitrobenzene (results compared with exposed nickel nanoparticles and nickel supported on carbon) leading to very promising results.

Based on the urea-glass route and the saccharide route, simple equipment and transition metals, it was possible to have a one-pot synthesize with scale-up possibilities towards new material that can be applied in catalysis and battery systems. On the basis of this thesis, future investigations and even numerous applications can accomplished. Further investigations will be made towards other ternary carbide nano-composites using the modified saccharide route.

7. References

[1] P.T.Anastas, J.C.Warner, *Green Chemistry: Theory and Practice*, Oxford University Press, New York, **1998**.

[2] P. T. Anastas, L. B. Bartlett, M. M. Kirchhoff, T. C. Williamson, *Catal Today* **2000**, *55*, 11-22.

[3] R. A. Sheldon, I. Arends, U. Hanefeld, *Green Chemistry and Catalysis*, 1 ed., WILEY-VCH, Weinheim, **2007**.

[4] E.Hornbogen, H.P.Warlimont, *Metalle*, 5 ed., Springer DE, Berlin Heidelberg, **2006**.

[5] V. Polshettiwar, B. Baruwati, R. S. Varma, *Green Chem* **2009**, *11*, 127-131.

[6] H. Goesmann, C. Feldmann, *Angew Chem Int Edit* **2010**, *49*, 1362-1395.

[7] H. Hildebrand, K. Mackenzie, F. D. Kopinke, *Chemie Ingenieur Technik* **2007**, *79*, 1461-1462.

[8] J. Liu, Q. M. Pan, *Electrochem Solid St* **2010**, *13*, A139-A142.

[9] D. J. Ham, J. S. Lee, *Energies* **2009**, *2*, 873-899.

[10] F. Alonso, I. Osante, M. Yus, *Tetrahedron* **2007**, *63*, 93-102.

[11] B. Bridier, J. Perez-Ramirez, *J Am Chem Soc* **2010**, *132*, 4321-4327.

[12] D. Astruc, *Nanoparticles and Catalysis, Vol. 1*, Wiley-VCH, Weinheim, **2008**.

[13] S. Glatzel, Dissertation thesis, Universität Potsdam (Potsdam), **2013**.

[14] Y. Abu-Lebdeh, I. Davidson, *Nanotechnology for Lithium-Ion Batteries*, Springer, New York, Heidelberg, Dordricht, London, **2012**.

[15] B. Milke, Dissertation thesis, Universität Potsdam (Potsdam), **2012**.

[16] S. T. Oyama, *Catal Today* **1992**, *15*, 179-200.

[17] C. Giordano, M. Antonietti, *Nano Today* **2011**, *6*, 366-380.

[18] S. T. Oyama, J. C. Schlatter, J. E. Metcalfe, J. M. Lambert, *Ind Eng Chem Res* **1988**, *27*, 1639-1648.

[19] O. Ambacher, *J Phys D Appl Phys* **1998**, *31*, 2653-2710.

[20] C. Giordano, C. Erpen, W. T. Yao, B. Milke, M. Antonietti, *Chemistry of Materials* **2009**, *21*, 5136-5144.

[21] C. Giordano, T. Corbiere, *Colloid and Polymer Science* **2012**.

[22] H.-D. Dörfler, *Grenzflächen und kolloid-disperse Systeme: Physik und Chemie*, Springer DE, Berlin Heidelberg, **2002**.

[23] I. M. Watt, *The Principles and Practice of Electron Microscopy*, 2 ed., Cambridge University Press, Cambridge, **1997**.

[24] D. B. Williams, C. B. Carter, *Transmission Electron Microscopy: A Textbook for Materials Science, Vol. 1*, 2 ed., Springer, New York, **2009**.

[25] J. Brehm, *Synthese und Charakterisierung nanokristalliner transparenter Halbleiteroxide*, 1 ed., Cuvillier Verlag, Göttingen, **2005**.

[26] A. I. Kirkland, J. L. Hutchison, *Nanocharacterisation*, Royal Society of Chemistry, Cambridge, **2007**.

[27] D. A. Skoog, J. J.Leary, *Instrumentelle Analytik*, Springer, Berlin-Heidelberg, **1996**.

[28] K. S. W. Sing, *Pure Appl Chem* **1982**, *54*, 2201-2218.

[29] http://www.elementar.de/en/products/applications/chnos-elemental-analysis/vario-el-cube.html, **access: 02.13.2013**.

[30] E. Riedel, C. Janiak, *Anorganische Chemie*, 7 ed., Walter de Gruyter, Berlin, **2007**.

[31] http://www.thalesnano.com/products/h-cube, **access: 02.13.2013**.

[32] M. C. McMaster, *GC/MS: A Practical User's Guide*, 2 ed., Wiley-Interscience, New Jersey, **2008**.

[33] K. Nogi, M. Hosokawa, M. Naito, T. Yokoyama, *Nanoparticle Technology Handbook*, 2 ed., Elsevier, Oxford, **2012**.

[34] H. K. Schmidt, *Chemie in unserer Zeit* **2001**, *35*, 176-184.

[35] B. L. Cushing, V. L. Kolesnichenko, C. J. O'Connor, *Chem Rev* **2004**, *104*, 3893-3946.

[36] M. Niederberger, N. Pinna, *Metal Oxide Nanoparticles in Organic Solvents*, Springer, Dordrecht, Heidelberg, London, New York, **2009**.

[37] B. M. Eick, J. P. Youngblood, *J Mater Sci* **2009**, *44*, 1159-1171.

[38] B. Milke, C. Wall, S. Metzke, M. Fichtner, C. Giordano, *Chem.Mat.* **2013 (submitted)**.

[39] C. Wall, S. Metzke, B. Milke, C. Giordano, M. Fichtner, **2013 (in progress)**.

[40] X. Liu, M. Krott, P. Müller, C. Hu, H. Lueken, R. Dronskowski, *Inorg Chem* **2005**, *44*, 3001-3003.

[41] C. H. Hamann, W. Vielstich, *Elektrochemie*, 4 ed., WILEY-VCH, Weinheim, **2005**.

[42] F. Badway, N. Pereira, F. Cosandey, G. G. Amatucci, *J Electrochem Soc* **2003**, *150*, A1209-A1218.

[43] A. J.Bard, G. Inzelt, *Electrochemical Dictionary*, 2nd ed., Springer, Berlin Heidelberg, **2012**.

[44] H. Q. Yang, H. Al-Brithen, E. Trifan, D. C. Ingram, A. R. Smith, *J Appl Phys* **2002**, *91*, 1053-1059.

[45] R. Schenck, A. Kortengraber, *Z Anorg Allg Chem* **1933**, *210*, 273-285.

[46] M. D. Lyutaya, A. B. Goncharuk, *Powder Metall Met Ceram* **1977**, *16*, 208-212.

[47] J. W. Huang, J. Li, H. Peng, *Powder Metall* **2007**, *50*, 137-141.

[48] Q. Hao, L. Q. Xu, G. D. Li, Z. C. Ju, C. H. Sun, H. Y. Ma, Y. T. Qian, *J Alloy Compd* **2011**, *509*, 6217-6221.

[49] X. Fang, X. Lu, X. Guo, Y. Mao, Y.-S. Hu, J. Wang, Z. Wang, F. Wu, H. Liu, L. Chen, *Electrochem Commun* **2010**, *12*, 1520-1523.

[50] Q. Sun, Z.-W. Fu, *Appl Surf Sci* **2012**, *258*, 3197-3201.

[51] J. Y. Yuan, C. Giordano, M. Antonietti, *Chemistry of Materials* **2010**, *22*, 5003-5012.

[52] A. Oya, S. Otani, *Carbon* **1979**, *17*, 131-137.

[53] I. Mochida, R. Ohtsubo, K. Takeshita, H. Marsh, *Carbon* **1980**, *18*, 117-123.

[54] R. Prakash, C. Wall, A. K. Mishra, C. Kubel, M. Ghafari, H. Hahn, M. Fichtner, *J Power Sources* **2011**, *196*, 5936-5944.

[55] W. Luo, Y. Xie, C. Z. Wu, F. Zheng, *Nanotechnology* **2008**, *19*.

[56] in *NIST X-ray Photoelectron Spectroscopy Database, Vol. 4.1*, National Institute of Standards and Technology, Gaithersburg, **2012**.

[57] B. Lu, X. D. Liu, K. Nakatsuji, T. Iimori, F. Komori, *Phys Rev B* **2007**, *76*.

[58] M. A. Pimenta, G. Dresselhaus, M. S. Dresselhaus, L. G. Cancado, A. Jorio, R. Saito, *Phys Chem Chem Phys* **2007**, *9*, 1276-1291.

[59] Y. Xu, M. Mahmood, Z. R. Li, E. Dervishi, S. Trigwell, V. P. Zharov, N. Ali, V. Saini, A. R. Biris, D. Lupu, D. Boldor, A. S. Biris, *Nanotechnology* **2008**, *19*.

[60] S. Reich, C. Thomsen, *Philos T R Soc A* **2004**, *362*, 2271-2288.

[61] in *Raman Spectra Database of Minerals and Inorganic Materials*, National Institute of Advanced Industrial Science and Technology (AIST), **2008**.

[62] D. S. Bem, C. M. Lampe-Önnerud, H. P. Olsen, H. C. zur Loye, *Inorg Chem* **1996**, *35*, 581-585.

[63] C. Heitner, D. Dimmel, J. Schmidt, *Lignin and Lignans: Advances in Chemistry*, CRC Press Taylor & Francis Group, Florida, **2010**.

[64] S. J. Lee, J. Jung, M. A. Kim, Y. R. Kim, J. K. Park, *J Mater Sci* **2012**, *47*, 8112-8117.

[65] A. Leineweber, H. Jacobs, *J Alloy Compd* **2000**, *308*, 178-188.

[66] J. Weber, M. Antonietti, A. Thomas, *Macromolecules* **2008**, *41*, 2880-2885.

[67] D. Esposito, M. Antonietti, *Chemsuschem* **2013**, *6*, 989-992.

[68] P. Isfort, T. Penzkofer, E. Pfaff, P. Bruners, R. W. Gunther, T. Schmitz-Rode, A. H. Mahnken, *Cardiovasc Inter Rad* **2011**, *34*, 833-838.

[69] M. Crespo-Quesada, F. Cardenas-Lizana, A. L. Dessimoz, L. Kiwi-Minsker, *Acs Catal* **2012**, *2*, 1773-1786.

[70] P. Rylander, *Catalytic Hydrogenation over Platinum Metals*, Elsevier, **1967**.

8. Appendix

8.1. List of abbreviations

Ac	acetate (CH_3COO^-)
BET	*Brunauer-Emmett-Teller* (nitrogen sorption)
EDX	energy dispersive X-ray spectroscopy
EELS	electron energy-loss spectroscopy
FWHM	full width at half maximum
GC-MS	gas chromatography with mass spectrometry
HRTEM	high resolution transmission electron microscopy
ICDD	International Center for Diffraction Data
NIR	near infra-red
$SA_{BET, app.}$	Apparent BET surface area
SAED	selected area electron diffraction
SEM	scanning electron microscopy
TEM	transmission electron microscopy
wt%	weight percent
XRD	X-ray diffraction (wide angle)

8.2. Chemicals

1 M LiPF6 in EC:DMC (1:1) (Merck, LP30); Aluminium nitrate nonahydrate (Sigma, 98-102%); Ammonium metatungstate hydrate (ABCR, 99.9%); carbon black (Alfa Aesar); Cellulose (Aldrich); Copper(II) chloride dehydrate (Aldrich, 99%); Ethanol (VWR, absolute, 99.9%); Formic acid (Sigma, 95%); Glucose (Sigma); Guanidine actetate (Aldrich); Iron(II) acetate (ABCR, anhydrous, 97%); Iron(III) nitrate nonahydrate (Alfa/Sigma, 98+%); Lignin (self-extracted, impure); lithium foil (Goodfellow, 99.9%); Manganese acetate tetrahydrate (Sigma-Aldrich, 99%); Methanol (Merck, 99.9%); Nickel(II) nitrate hexahydrate (Roth, ≥99%); Nitrobenzene (Fluka, 99%); N-Methyl-2-pyrrolidone (Alfa Aesar); Palladium(II) chloride (Applichem, >59% palladium); Palladium(II) nitrate hydrate (Aldrich, 37.0 - 42.0% palladium); PVDF binder (Solef); Sucrose (Sigma , 99.5%); Urea (Sigma, 99-100.5%).

All chemicals were used without further purification.

8.3. Analytical equipment

Elemental Analysis

Elemental analysis was performed using a Vario EL Elementar. During the high temperature extraction, the solid samples were put into a gas phase before they are separated into their components.

GC-MS

Analysis by GC-MS was performed with a 5975 Gas Chromatograph (Agilent Technologies) with a MS detector and a capillary column (HP-5MS, 30 m, 0.25 mm, 0.25 micron). Starting with an isothermal step at 50 °C for 2 min, the temperature program then increased with a rate of 30 K/min to 300 °C and maintained for 1 min. Signal evaluation was done by using the MS library NIST 08 database with a retention index allowance of ±100.

Hydrogenation reactor

Catalytic tests were carried out using an H-Cube Pro Continuous-flow Hydrogenation reactor (ThalesNano) with a flow of 0.3 – 0.5 mL/min and a pressure of 12 bar.

HRTEM

High resolution TEM was performed at a Philips CM 200 LaB_6 using an acceleration voltage of 200 kV.

ICP-OES

Inductively coupled plasma optical emission spectrometry measurements were performed at a VISTA-MPX (Varian) using an argon plasma. Sample preparation was performed using an air oven and burning the samples for 36 h at 500 °C in order to destroy the carbon matrix. Afterwards the samples were dissolved in aqua regia and diluted before the measurement.

NIR-Raman

Near infra-red Raman measurements were performed using a confocal Raman microscope (CRM200, WITec) supplied with a piezo-scanner (P-500, Physik Instrumente). The 785 nm near infra-red laser excitation (diode pumped, linearly-polarized, Toptica Photonics AG) was combined with a x20 microscope objective (Nikon, NA = 0.4). The spectra were obtained using an air-cooled CCD (PI-MAX, Princeton Instruments Inc.). ScanCtrlSpectroscopyPlus software (version 1.38, Witec) was used for measurement setup and spectra processing.

Nitrogen Sorption

Nitrogen Sorption measurements were performed with a Quantachrom Quadrasorb instrument at liquid nitrogen temperature (-196 °C). All samples were degassed for 20 h at 150 °C before the measurement. Data evaluation was done by Quantachrom QuadraWin Software (version 5.05).

Oven

All calcination reactions were performed using an annealing furnace (Nabertherm, N7/H) under a constant nitrogen flow. The sample preparation for ICP-OES was performed in a smaller furnace (Nabertherm, L3/11) under air.

SEM

SEM measurements were performed using a LEO 1550 Gemini Instrument. The samples were prepared by placing them on a carbon coated aluminium stub. The samples were measured without sputtering, since they were already conductive.

TEM

TEM measurements were performed at a Zeiss EM 912Ω with an acceleration voltage of 120 kV. Some droplets of the sample's dispersion in ethanol were put unto a 400 mesh carbon-coated copper grid for sample preparation. Ultramicrotomes were received by embedding the samples in LR White Resin (medium grade, Agar Scientific) and cutting them with a Leica Ultracut UTC. The cuts were also put unto a 400 mesh carbon coated copper grid.

XRD

X-ray diffraction measurements were performed using a D8 diffractometer by Bruker Instruments (Cu Kα-radiation, λ=0.154 nm) and using a scintillation counter (Kevex detector). All reference patterns were assigned by Match! Software using the ICDD-PDF4+ database (2011 and 2012 edition).

Data evaluation was carried out using Origin 8.6 and Origin Pro 9.0; Microscopy evaluation was done using Digital Micrograph 3.7 and ImageJ 1.44.

9. Acknowledgements

This work would not have been possible without the loyal help from so many people around me. Let me send you an affectionate 'Thank you!'.

At first I want to thank Dr. Cristina Giordano, who gave me a place in her research group, a fascinating topic and tons of advice at all times. I also want to thank her for being the examiner of my master thesis.

The great research opportunities and the wide equipment were offered to me by the Max Planck Institute of Colloids and Interfaces in Golm. Therefore I want to give thanks to Professor Markus Antonietti, who, as the leader of the department for colloid chemistry, believed in my abilities during research.

Of course I really have to thank Prof. Andreas Taubert who agreed being the second examiner of my master thesis.

For the alkylation catalysis testing and the nitrogen sorption measurements of the cellulose-based compounds, my thanks go to Prof. Rafael Luque (Universidad de Córdoba) and also to Clemens Wall from the Karlsruhe Institute of Technology (KIT) for the battery tests.

I am very grateful to Guylhaine Clavel for the advice she gave me (not only) concerning TEM and for the numerous measurements including HRTEM, EELS and EDX that she performed at the Fritz-Haber-Institut in Berlin and to which my thanks are also going to.

For the introduction to Raman-techniques, the hydrogenation catalysis testing and fresh ideas I give my thanks to Valerio Molinari.

I do not want to forget all the employees and researchers at the Max Planck Institute who did various analytical investigations including the TEM-Ultramicrotomy and elemental analysis for me and who contributed to a nice working atmosphere. I would like to thank Debora Ressnig for the ICP measurements, Irina Shekova, Dr. Jens Weber, and Katharina Otte for the help with the nitrogen sorption measurements and Dr. Xiaofeng Liu for the SEM investigations that he carried out for me.

At last I want to thank Katharina, Jessica, Nora, Patrick and Claudia for being friends to me during the time in the institute. It was a great pleasure spending my time with you.

10. Selbstständigkeitserklärung / Declaration of Authorship

Hiermit erkläre ich, dass ich die vorliegende Masterarbeit selbstständig und ohne Hilfe verfasst und keine anderen als die angegebenen Hilfsmittel und Quellen benutzt habe. Wörtlich oder inhaltlich entnommene Stellen habe ich als solche kenntlich gemacht.

Potsdam, 14.Oktober 2013

I herewith formally declare that I myself have independently written the submitted Master thesis. I did not use any outside support except for the cited literature and all the other quoted sources which I employed producing this academic work, either literally or in content.

Potsdam, 14th of October 2013

Sarah Metzke